JOURNAL OF GEOPHYSICAL RESEARCH: OCEANS, VOL. 118, 6329–6348, doi:10.1002/2013JC009189, 2013

Wave power variability and trends across the North Pacific

Peter D. Bromirski,[1] Daniel R. Cayan,[2] John Helly,[3] and Paul Wittmann[4]

Received 7 June 2013; revised 13 September 2013; accepted 4 October 2013; published 2 December 2013.

[1] Multiyear climate variations influence North Pacific storm intensity and resultant variations in wave energy levels. The timing of these decadal fluctuations and strong El Niño's have had a strong influence on long-term trends. Here we investigate variations in the North Pacific wave power, P_W, determined from WAVEWATCH III (WW3) wave model significant wave height, *Hs*, and peak period data forced by NRA-1 winds spanning the 1948–2008 epoch. Over the entire hindcast, upward trends in *Hs* and P_W, especially in winter, are observed over much of the North Pacific, strongly influenced by an apparent storm intensification after the mid-1970s regime shift. Heightened P_W is concentrated in particular regions of the basin, and is associated with increased wave activity during the warm phase of the Pacific Decadal Oscillation (PDO). Wave power events, P_E, defined as episodes when *Hs* exceeded the 90th percentile threshold for at least 12 h, exhibit significant upward trends along much of the U.S. Pacific coast during winter months. Importantly, the hindcast exhibits a recent decrease in P_W across much of the North Pacific, in contrast to the long-term increase of P_W and *Hs*. This recent decrease is associated with the prevalent PDO cool phase that developed after the late 1990s. Variability and intensification of coastal P_W and P_E have important practical implications for shoreline and beach erosion, coastal wetlands inundation, storm-surge flooding, and coastal planning. These considerations will become increasingly important as sea level rises.

Citation: Bromirski, P. D., D. R. Cayan, J. Helly, and P. Wittmann (2013), Wave power variability and trends across the North Pacific, *J. Geophys. Res. Oceans*, *118*, 6329–6348, doi:10.1002/2013JC009189.

1. Introduction

[2] Surface gravity waves provide much of the energy that drives physical processes along coasts. The greatest societal impacts result when high waves occur near high tide, producing coastal flooding as well as beach and sea cliff erosion, affecting coastal infrastructure. Because the simultaneous occurrence of high waves and high tide produces the greatest coastal impacts, the duration of extreme wave events along coastlines is a significant factor. Impacts of wave activity in coastal regimes will be exacerbated by anticipated global warming-related sea level rise, which allows more wave energy to reach farther shoreward. Increases or decreases in wave power and their characteristics along coasts are thus important for mitigation and adaptation planning.

[3] Changes in the wave climate across the North Pacific have mostly focused on the distribution and trends in significant wave height (*Hs*, the average of the highest 1/3 of the waves), either by analyses of buoy data [*Graham and Diaz*, 2001; *Bromirski et al*., 2005] or wave model hindcasts [*Graham and Diaz*, 2001; *Cox and Swail*, 2001; *Wang and Swail*, 2001].

[4] Identifying reliable trends in regional wave activity from buoy data analyses are limited because they are sparse point measurements, many of which are contaminated by instrumental problems. Recently, *Gimmrich et al*. [2011] identified systematic problems in NOAA buoy records that call into question the validity of *Hs* and wave spectral energy trend estimates made using uncorrected buoy data. This is particularly important in the North Pacific where El Niño-Southern Oscillation (ENSO)-related wave-climate variability produces elevated interannual wave conditions that can strongly affect trend analyses. Modulation of ENSO teleconnections by the phase of the Pacific decadal oscillation (PDO) [*Mantua et al*., 1997] may be important [*Gershunov and Barnett*, 1998]. Pronounced decadal variability in North Pacific storminess [*Bromirski et al*., 2003; *Mantua and Hare*, 2002; *Latif and Barnett*, 1994; *Trenberth and Hurrell*, 1994] further introduces uncertainty in *Hs* trends derived from relatively short buoy time series.

Additional supporting information may be found in the online version of this article.

[1]Climate, Atmospheric Sciences, and Physical Oceanography Division, Scripps Institution of Oceanography, University of California, San Diego, La Jolla, California, USA.

[2]Climate Research Division, Scripps Institution of Oceanography and U.S. Geological Survey, La Jolla, California, USA.

[3]San Diego Supercomputer Center and Scripps Institution of Oceanography, University of California, San Diego, Climate Research Division, La Jolla, California, USA.

[4]Fleet Numerical Meteorology and Oceanography Center, Monterey, California, USA.

Corresponding author: P. D. Bromirski, Climate, Atmospheric Sciences, and Physical Oceanography Division, Scripps Institution of Oceanography, University of California, San Diego, 9500 Gilman Drive, La Jolla, CA 92093-0209, USA. (pbromirski@ucsd.edu)

2169-9275/13/10.1002/2013JC009189

[5] Objective reanalysis methodologies that produce the wind fields, which force wave models, have their own sources of uncertainty in addition to observational errors [*Caires et al*., 2004; *Sterl*, 2004; *Chang*, 2007], not the least of which stems from changes in Reanalysis data assimilation in 1979 resulting from the introduction of satellite observations. However, wave model hindcasts driven by reanalysis wind fields have produced reasonably good agreement with buoy measurements [*Cox and Swail*, 2001; *Graham and Diaz*, 2001; *Caires et al*., 2004], and have been useful in studying broad-scale patterns over a range of time scales from synoptic to multidecadal, including trends. The advantages of wave model hindcasts over buoy observations include their comprehensive spatial coverage and their consistent response to wind-forcing over time, allowing for comparative trend analyses across basins. Evidence from a series of studies underscores the important role of interannual to interdecadal variation in the North Pacific wave climate [e.g., *Graham and Diaz*, 2001; *Storlazzi and Griggs*, 2000; *Bromirski et al*., 2005]. Furthermore, there is some evidence for multidecadal trends in wave heights, indicated by buoy observations [*Gemmrich et al*., 2011; *Seymour*, 2011] and from remote-sensed observations [*Young et al*., 2011]. This evidence motivates consideration of a relatively long, continuous hindcast simulation of North Pacific waves to investigate the variability and consider possible trends.

[6] Because storm impacts on coastal processes depend in part on the energy that is delivered by waves, it is illuminating to consider peak wave period, *Tp* (the wave period of the maximum spectral energy density), as well as *Hs*. These two measures are needed to estimate wave power, P_W, which increases nonlinearly with *Hs* and is proportional to *Tp*. Wave power is a better descriptor of storm strength than *Hs* alone, providing an estimate of storm event wave intensity. *Tp* depends on both the duration and area (fetch) that persistent winds blow across, as well as wind speed, and is an important factor in the magnitude of coastal impacts. Locally generated wind waves have $Tp < 10$ s, while swell generated under large Pacific storms typically have $Tp > 16$ s. Higher *Tp* waves produce higher wave runup, which increases flooding potential [*Stockdon et al*., 2006; *Bromirski et al*., 2012]. Larger, more intense extratropical cyclones (ETCs) generate longer period waves. The wave power measure allows comparison of changes in storm event characteristics. For example, wave power variability in the western North Atlantic has been associated with hurricane intensity in the basin [*Bromirski and Kossin*, 2008]. Coastal inundation depends on *Hs* and *Tp*, as well as timing relative to high tide, so fluctuations and trends of strong wave power events have a direct application. These are crucial considerations in adapting to and mitigating impacts from changing storm characteristics and patterns as a result of global warming.

[7] Previous analyses of wave model hindcasts have generally focused on *Hs* trends and the distribution and magnitude of extremes [*Wang and Swail*, 2001], not considering the important aspects of wave period and event duration, although wave energy fluxes in the Southern Hemisphere have recently been studied [*Hemer et al*., 2010]. From a coastal impacts perspective, the wave energy during high intensity events is critically important, since longer duration storm events are more likely to produce high waves near high tide. Accordingly, this study investigates spatial patterns, multiyear variability and trends in wave power in addition to *Hs*, and related aspects of extreme high wave events using wave model data spanning 1948–2008. The scope of this study is the entire North Pacific basin, but an emphasis is Eastern North Pacific wave activity, in view of the numerous impacts on societal and natural systems along the Pacific coast of North America.

[8] The paper is structured as follows. First the data and analysis methods are described, with comparison of the wave model *Hs* against buoy *Hs* to validate the model data. Then the spatial distributions of *Hs*, *Tp*, and P_W over the North Pacific during both winter and summer seasons are described, establishing trends of both the long-term mean and heightened levels of these wave characteristics. Their spatial distribution is described using empirical orthogonal functions, and the associations with well-known patterns of climate variability are determined from correlations of the associated principal components. Next, two different designations of wave events, those exceeding the 90th percentile *Hs* threshold and those most extreme winter and summer events of each year, are investigated, including a description of their spatial distribution, duration, associated P_W, and their trends. Finally, regional and eastern North Pacific wave power variability and its relationship to broad-scale climate patterns are explored.

2. Data and Methods

2.1. Wave Model Data

[9] A hindcast of ocean gravity wave heights spanning the 1948–2008 time period were generated with the WAVEWATCH III version 3.14 (WW3) [*Tolman*, 2009] wave model. The WW3 wave model was run over a global domain forced by NOAA National Centers for Environmental Prediction (NCEP) reanalysis project [*Kalnay et al*., 1996] global near-surface winds (NRA-1), nominally at 10 m elevation. Global *Hs* and *Tp* wave parameter outputs were saved at 6 h intervals with a spatial resolution of 1.0° × 1.0° latitude/longitude. This study considers only the North Pacific wave output from this hindcast, a subset of the WW3 global model domain, although waves generated south of the analysis domain are necessarily included in the analyses.

[10] Gaps in buoy records from nonoperation (e.g., Figures 1c and S2–S4), not uncommon during other years not examined here, obscure efforts to establish reliable long-term trends from buoy records. Furthermore, gaining an understanding of Pacific wave variations, particularly their trends, from buoy estimates is challenged in several ways: (1) the much shorter buoy record (generally beginning in the early 1980s) compared to WW3 model *Hs* (beginning 1948), (2) large interannual fluctuations, such as the heightened wave activity during strong ENSO episodes [*Bromirski et al*., 2005] may significantly influence trends, especially if records are short, (3) the sparse buoy spatial coverage that inhibits reliable regional determinations, (4) the problems associated with multiple buoy platforms at the same location [*Gemmrich et al*., 2011], (5) buoy

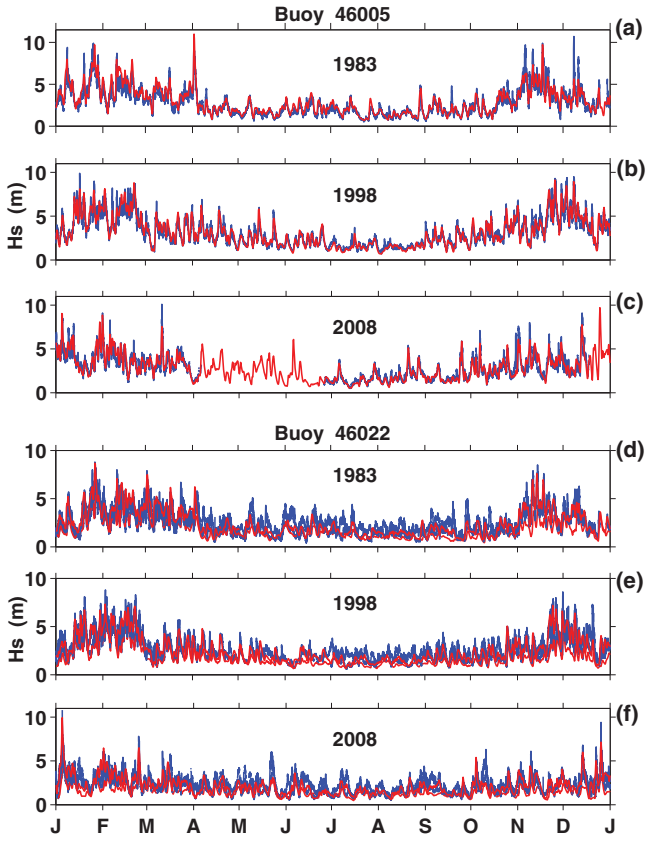

Figure 1. Comparison of WAVEWATCH III (WW3) wave model *Hs* forced by NRA-1 winds (red) at the nearest grid node to NOAA buoy *Hs* measurements (blue) during years 1983, 1998, and 2008 at (a–c) open-ocean buoy 46005 and at (d–f) near-coastal buoy 46022. See Figure 3a for locations.

transfer function calibration issues [*Steele et al*., 1985], and (6) several decade time series and complete spatial coverage are particularly important to investigate fluctuations and changes in the presence of significant interdecadal storminess variability [*Bromirski et al*., 2003].

[11] Together these factors motivate the present study, where we use a reanalysis-derived wind-driven wave model simulation, and suggest that the WW3 model data offer a more complete, and possibly more reliable, estimate of multiyear fluctuations and changes in regional wave patterns.

2.2. Analysis Methodologies

[12] In this study, we investigate variability and changes within a six-decade observationally based simulation of North Pacific wave activity. The following measures are considered:

Hs	significant wave height;
P_W	wave power;
T_P	peak wave period;
Hs_{90}	90th percentile significant wave height;
Tp_{90}	peak wave period of 90th percentile;
Pw_{90}	90th percentile wave power;
Hs_{90T}	Hs occurrences above the 90th percentile level during a given season;
Pw_{90T}	Pw occurrences above the 90th percentile level during a given season;
P_E	wave power event;
P_{Emax}	maximum wave power event.

[13] The wave power, P_W, in deep water along a unit length of wave crest was estimated from H_S and T_P at each grid node from

$$P_W \approx \frac{1}{2} Ec = \frac{\rho g^2}{32\pi} H_S^2 T_P, \quad (1)$$

where E is the wave energy and c is the wave phase speed [*Kinsman*, 1965]. T_P is sensitive to the duration and size of the fetch over which strong winds persist, i.e., the storm's size and intensity. T_P depends on storm size, sustained wind speed, and duration. Thus, in contrast to an investigation that is solely based on Hs, P_W variability provides a better characterization of storm wave intensity and impacts.

[14] Empirical orthogonal function (EOF) analyses were employed to identify the dominant Hs and P_W regions in the North Pacific, and to investigate regional and basin-wide variability from the EOF patterns and their principal component (PC) time series of anomalous P_W activity.

[15] Linear trends in several of the identified measures were calculated over the six-decade period of record. These trends were designated to be significantly different from zero if they met or exceeded the 95% significance level of a two-sided Student's t test linear regression null-hypothesis test [*Hines and Montgomery*, 1980].

3. Wave Model *Hs* Validation

[16] Consistency and reliability of the WW3 wave model hindcast over the North Pacific were evaluated from a number of perspectives in order to determine if there is meaningful anomalous variability that is related to fluctuations of well-known climate indices. *Change*s in the relationship between the wave variability and associated climate indices within the earlier and later portions of the record might indicate that there have been systematic, time-varying biases in the wave model forcing winds, which would contaminate estimates of long-duration trends.

[17] To investigate the consistency of the Reanalysis wind-driven hindcast, we first made a detailed comparison of WW3 and NOAA buoy Hs time series (Figure 1) at selected locations across the eastern North Pacific (shown in Figure 3a) during 1983, 1998, and 2008. These years were chosen because 1983 and 1998 represent high-amplitude El Niño wave years, with 1983 near the beginning of the buoy record in the North Pacific and 2008 providing comparisons between early and more recent data to determine the consistency of WW3/buoy relationships. The time series plots in Figure 1 exhibit strong agreement between Hs peaks in WW3 wave model and those from NOAA buoy records (also see Supporting information, Figures S2–S4, for additional detailed comparisons), indicating that the dominant temporal atmospheric pressure patterns associated with the NRA-1 model wind fields are generally well determined. However, WW3 model Hs generally tend to underestimate buoy Hs, particularly at near-coastal locations, likely partly the effect of local bathymetry and coastline configuration, NRA-1 underestimation of

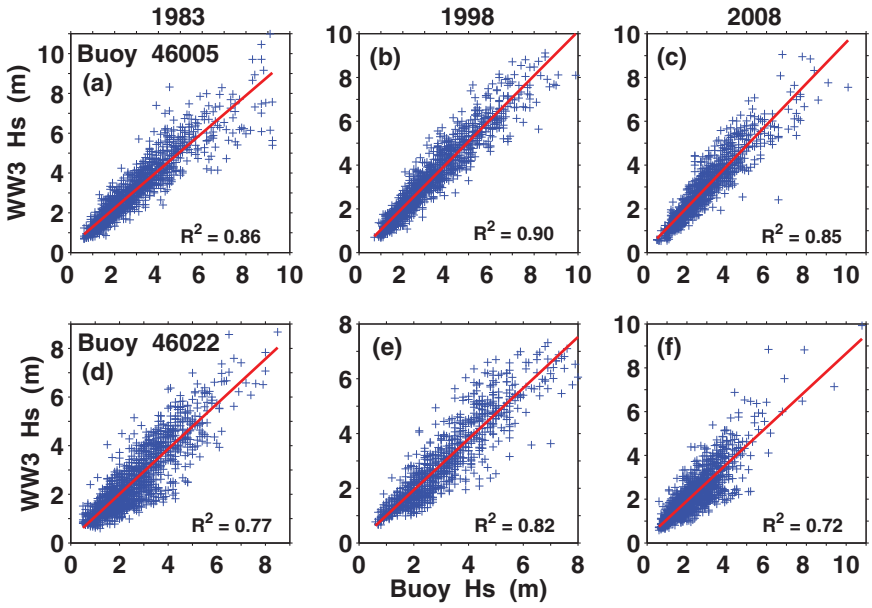

Figure 2. NOAA buoy *Hs vs* WW3 wave model *Hs* at the nearest WW3 grid node for the time series shown in Figure 1 during years 1983, 1998, and 2008 (see Figure 1) at (a–c) open-ocean buoy 46005 and at (d–f) near-coastal buoy 46022, with the correlation coefficient (r^2) for each comparison indicated. Least squaers trend lines (red) have slopes of (a–c) 0.94, 1.01, 0.94 and (d–f) 0.93, 0.93, 0.84, respectively. Slopes < 1 indicate WW3 model *Hs* underestimates buoy measurements. See Figure 3a for locations.

near-coastal eastern boundary wind fields, or being at the edge of the model domain. WW3 uses two types of global data sets: 2 min global bathymetry (this model run used ETOPO2; National Geophysical Data Center (NGDC) 2006 and Digital Bathymetric Data Base (DBDB2) v3.0; Naval Research Laboratory (NRL) 2006) and the global self-consistent hierarchical high-resolution shoreline (GSHHS) [*Wessel and Smith*, 1996]. Consequently, most coastal features are represented as subgrid obstructions. The resolution of the coastal bathymetry in ETOPO2 may contribute to differences between WW3 and buoy *Hs* since the relief that contributes to focusing of wave energy near the coast may not be adequately represented. However, because the difference between WW3 and buoy *Hs* varies with season and is more pronounced in summer, this suggests that issues with the eastern boundary wind field are likely primarily responsible for WW3 *Hs* underestimation at coastal locations.

[18] The underestimation of *Hs* at coastal locations is particularly evident during summer months, e.g., at 46022 (Figure 1d) and at 46011 (Figure S2a), and at the most southern coastal buoys 46023 and 46025 (Figure S2c). However, the relationships between WW3 and buoy *Hs* at 46005 and at 46002, both located in deep water near the eastern boundary of the model domain (e.g., Figures 1a–1c and S2a, respectively), suggest that near-coastal biases do not extend far offshore.

[19] To broaden this comparison, scatter plots between WW3 and buoy *Hs* were produced (Figures 2, S2b, S2d, S3b, S3d, S4b, and S4d). The scatter plots are reasonably tight, with high squared correlation coefficients (r^2), typically >0.80 at deep-ocean locations, that are consistent during each of the 3 years (1983, 1998, and 2008). Scatter plot least squares slopes are somewhat less than 1, indicating that WW3 model *Hs* tend to be less than buoy *Hs* estimates, with slopes generally shallower at near-coastal locations. Nevertheless, r^2 between WW3 and buoy *Hs* at near-coastal locations is still quite high, typically >0.7, indicating that *Hs* variability is well represented by WW3 model data. The least squares slopes typically <1 are in apparent contradiction to *Chang* [2007], who found that surface ship observations suggest that NRA-1 winds are biased high, which, if so, should produce WW3 estimates greater than buoy *Hs* observations, i.e., the slopes should be >1.

[20] *Hs* distributions are non-Gaussian, and are better described by Rayleigh distributions (Figure 3). Rayleigh distributions of WW3 and buoy *Hs* during winter (November to March) and summer (May to September) seasons over the 1981–2008 epoch show characteristic similarities and differences for respective aggregate WW3 *Hs* estimates. Comparisons between model and buoy *Hs* during winter (Figures 3b and 3c) show that, while buoy *Hs* is generally significantly higher than WW3 model estimates (as indicated in Figures 1, 2, and S2–S4), the shapes of the Rayleigh distribution curves for WW3 and the associated buoy *Hs* are similar. Furthermore, there are consistent WW3 versus buoy relationships between the different buoy locations, particularly at the deep-ocean sites. Purely Rayleigh distributions would track associated linear curves. The *Hs* distributions for both buoy and WW3 generally begin to significantly diverge from the theoretical linear trends near the 0.90 level, motivating selection of the 90th percentile level for strong event identification. The near-coastal WW3 *Hs* distributions (Figures 3d and 3e) diverge at somewhat lower levels.

[21] In using the WW3 simulation to study variability of North Pacific wave activity, it is crucial to ascertain that

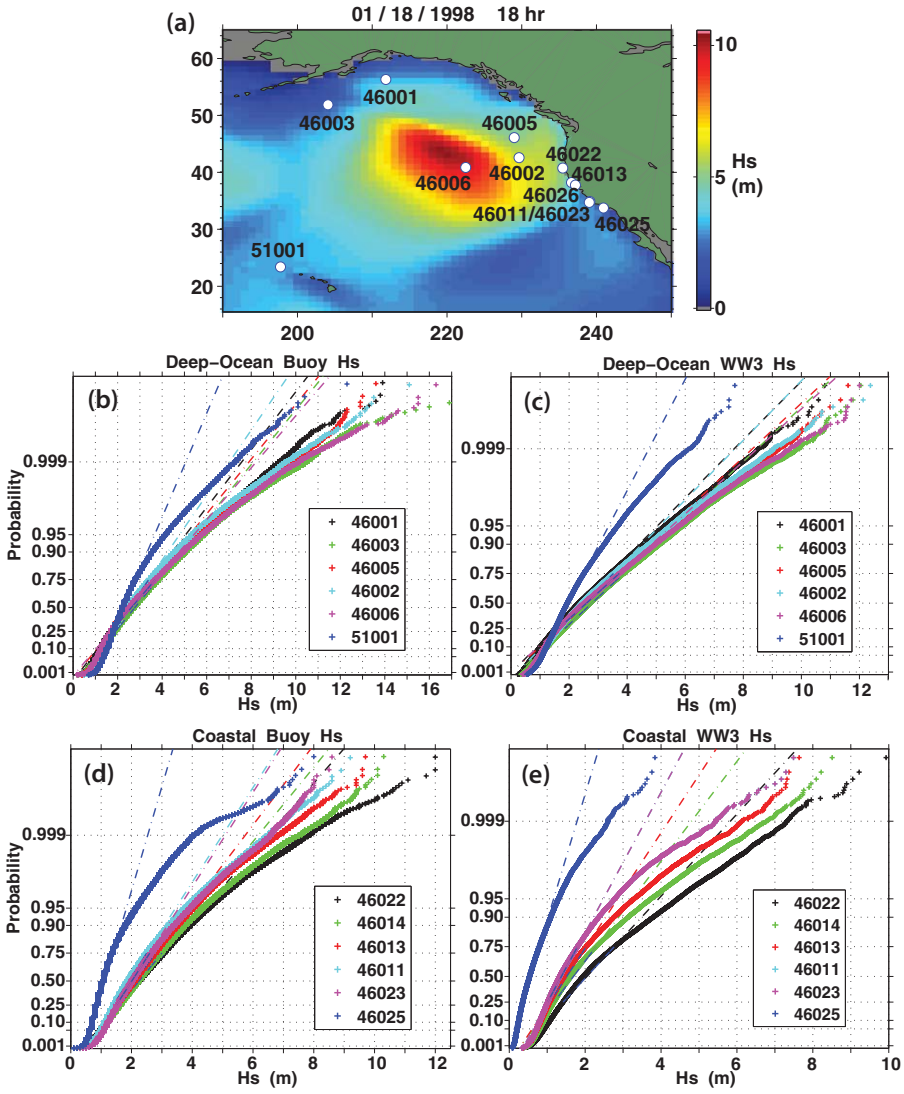

Figure 3. (a) WAVEWATCH III snapshot of *Hs* over the eastern North Pacific during 18 Jan. 1998 showing the locations of buoys used in WW3 *Hs* validation. Buoys 46013 and 46011 are located slightly north of 46026 and 46023, respectively. Near-coastal buoy 46014 (unlabeled) is located between 46013 and 46022. (b–d) Rayleigh exceedance probability distributions for winter *Hs*, comparing differences during winter between (b, d) NOAA buoy *Hs* and (c, e) WAVEWATCH III (WW3) wave model *Hs* forced by NCEP NRA-1 winds at grid nodes nearest respective buoys at deep ocean (top panels) and coastal (bottom panels, north-to-south) locations. Model *Hs* near 46011 in Figure 3e underlies that of nearby 46023. Associated theoretical Rayleigh distributions are represented by similarly-colored linear trend lines (dot-dashed).

the modeled *Hs* produces reliable spatial and temporal structure. Key to this issue is whether the relationships between model hindcast estimates and buoy observations are temporally and spatially consistent, which would suggest that WW3 is not impaired by artifacts that might lead to systematic biases or trends both over the buoy period from 1981 to 2008 and prior to the mid-1970s regime shift [*Miller et al*., 1994]. This comparison is particularly important because of potential spurious changes in atmospheric climate [*Chang*, 2007; *Sterl*, 2004], including the surface wind field, resulting from changes in observations and observation practices, such as the advent of remote-sensed information that were introduced into the Global Reanalysis in the late 1970s.

[22] Comparisons of WW3 and buoy *Hs* during winter (November to March, Figures 4a and 4c) and summer (May to September, Figures 4b and 4d) seasons over the 1981–2008 epoch, during which at least 50% of corresponding buoy observations were available, indicate that there are generally no statistically significant trends in the regression of the correlation slopes between model and buoy *Hs*. Although the correlation slopes between model and buoy *Hs* show substantial interannual variability, particularly at and between near-coastal buoys and buoy 51001 near Hawaii, the lack of statistically significant trends in the correlation slopes suggests that the WW3 model *Hs* are self consistent, i.e., trends in *Hs* do not appear to be strongly influenced by persistent biases in the WW3 estimates

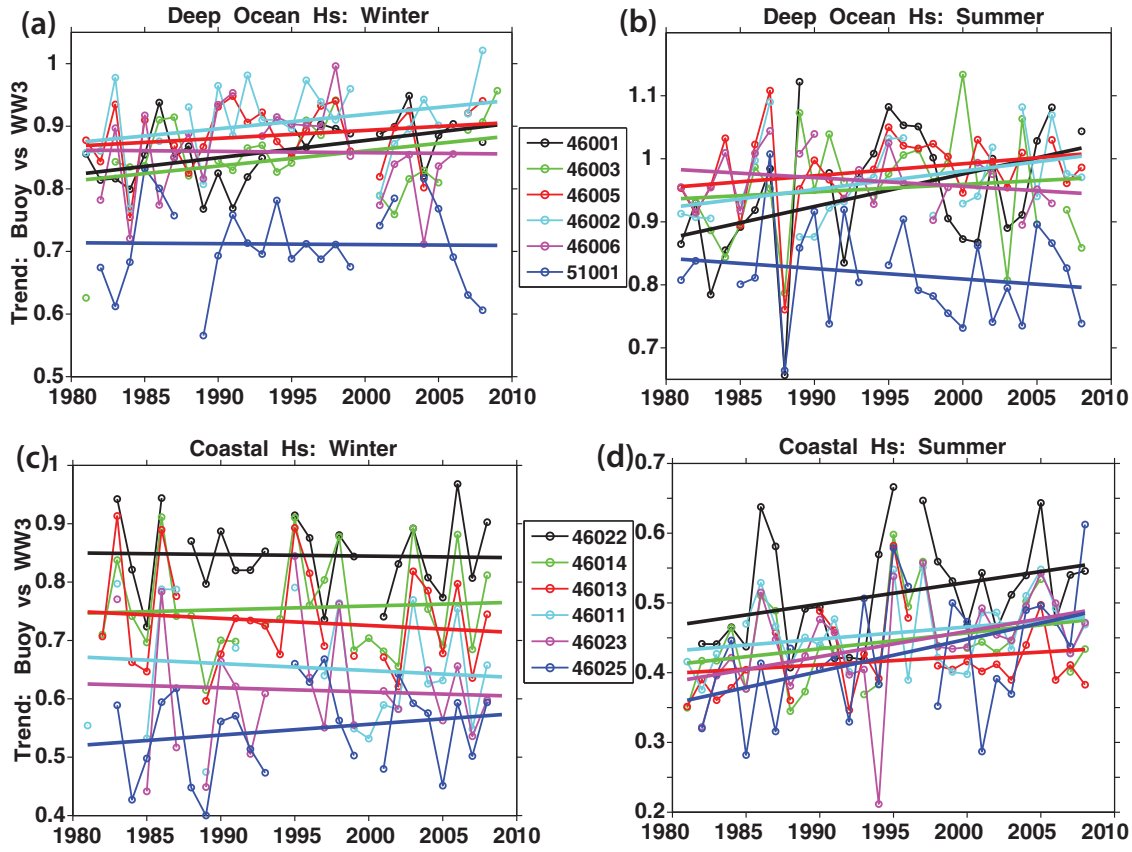

Figure 4. Trends in scatter-plot regression coefficients (as in Figure 2 and Figures S2b, S2d, S3b, S3d, S4b, and S4d) between buoy *Hs* and WW3 *Hs* during winter (left panels) and summer (right panels) at deep ocean (top panels) and near-coastal (bottom panels) locations. At least 50% of corresponding buoy observations during each season were required for seasonal inclusion. WW3 data were extracted at the grid node nearest respective NOAA buoy locations. Trends (thick linear lines) are statistically significant during winter only at 46001 (a), and during summer at 46001 (b), and 46023, 46025 (d).

relative to the buoy observations, at least not over seasonal time scales in the eastern North Pacific where buoy data are available. These relationships are consistent with the generally constant low level of inhomogeneities for reanalysis products in the Northern Hemisphere [*Sterl*, 2004]. The generally high correlations between WW3 and buoy observations, particularly at deep-ocean locations, reflect the strong association of heightened wave activity and storminess with broad-scale atmospheric circulation patterns [*Bromirski et al*., 2003, 2005] that are likely well characterized by NRA-1 winds.

[23] Next, to evaluate the consistency of model *Hs* between buoy and prebuoy epochs, we investigated empirical orthogonal functions (EOFs) of the WW3 monthly *Hs* anomaly series. The EOFs are calculated separately for the 1948–1977 and 1978–2008 epochs (Figure 5), before and after the mid-1970s regime shift [*Miller et al*., 1994]. Available buoy observations are limited to the period after the 1977 climate shift, so comparison of the variability across the two epochs is useful to evaluate the veracity of the model simulation during the earlier, buoy-void period. The first three EOF modes account for about 50% of the variance in both epochs. The spatial patterns of the first three modes for both epochs are very similar. The spatial pattern of mode 1 reflects the dominant influence of variability of the Aleutian Low/Gulf of Alaska Low complex on storm systems across the North Pacific. In the latter epoch, mode 1 undergoes an eastward and slightly southward intensification. Mode 2, a southwest-northeast dipole pattern, evolves into a more pronounced east-west pattern in the latter epoch, with the dominant pole shifted westward. Mode 3, a north-south pattern, also becomes more pronounced during the latter epoch, with an apparent clockwise rotation. However, the overall makeup of the three modes is strikingly similar before and after the 1970s shift, indicating that the variability derived from the NRA-1 forcing winds has relatively consistent spatial and temporal structure. Taken together, the relatively subtle shifts of the first three modes reflect a transition toward heightened wave activity across the North Pacific basin, including the region along the Pacific coast of North America, as will be described in subsequent sections.

[24] Correlations of the principal component time series (PC1, PC2, PC3) of the first three monthly *Hs* anomaly modes with monthly climate indices over the pre- and post-1977 regime shift (to the warm phase of the PDO) epochs provides a test to determine whether the wave variations are affected by Pacific climate fluctuations consistently over the time period covered by the NRA-1 forcing and the WW3 simulation. Climate indices that are commonly used

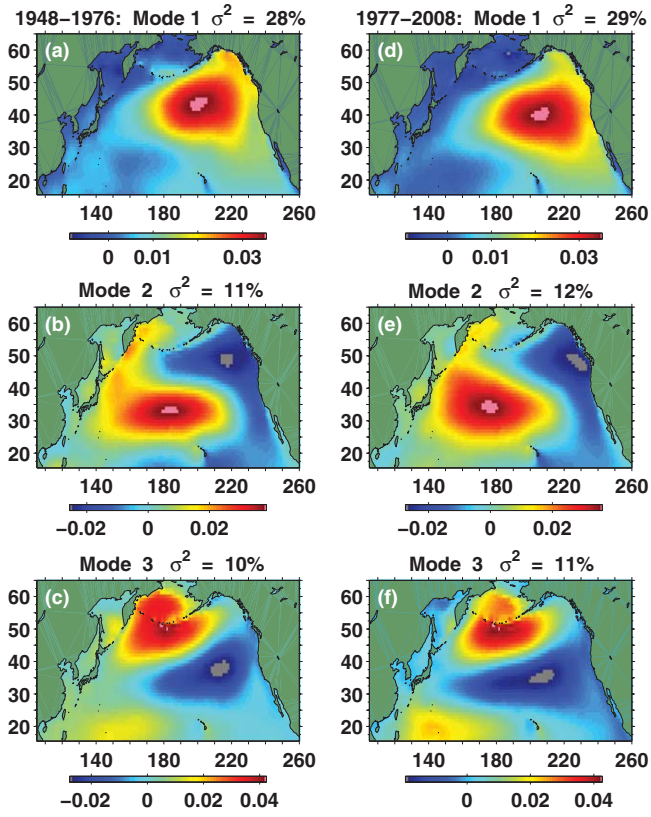

Figure 5. Comparison of *Hs* EOF spatial structures for modes 1, 2, and 3 for earlier (pre-1976) and later (post-1976) epochs of the WW3 model record, determined from monthly *Hs* anomalies (formed from the difference between the monthly mean and the climatological mean, for all months (Jan.–Dec.) at each grid point) normalized to unit variance. EOFs were scaled to identify peaks (maxima in red), with colorbars indicating relative weights. The percent variance explained by each mode is indicated in each panel title. Note the shadowing effect of the Hawaiian Islands.

to describe modes of climate variability across the North Pacific include the multivariate ENSO index (MEI) [*Wolter and Timlin*, 1998], the North Pacific pressure pattern (NP) [*Trenberth and Hurrell*, 1994], and the Pacific North America pattern (PNA) [*Wallace and Gutzler*, 1981], and SST-derived indices NINO3.4 [e.g., *Kumar and Hoerling*, 2003] and the Pacific decadal oscillation (PDO) [*Mantua et al.*, 1997]. The significant correlations of PC1 with all climate indices during the pre- and post-1977 epochs during winter (Table 1) indicate consistent relationships with *Hs* across the entire model record. Although the atmospheric pressure-derived NP and PNA indices are associated with NRA-1 winds, both the PDO and NINO3.4 (defined as the average of SST anomalies over the region 5°N–5°S and 170°–120°W) indices are determined from North Pacific and tropical Pacific Sea Surface Temperature (SST), and thus are less closely related to wind data. While SST and winds are linked [*Bromirski et al.*, 2011], they are less directly associated than atmospheric pressure patterns and wind, and SST is observed separately and independently from winds or atmospheric pressure. Thus, similar correlations of atmospheric circulation and the SST-derived indices with PC1 over the two epochs, that exhibit similar spatial structures and magnitudes, suggest that the pattern of variability in NRA-1 forced model winds has remained consistent. The improved correlation of PC3 with the circulation and the NINO3.4 indices for the 1978–2008 epoch compared to the 1948–1977 epoch during winter suggests a more pronounced influence on the north-south *Hs* variation across the basin, perhaps in association with the warm phase of the PDO.

[25] During summer, *Hs* PC correlations (Table 1) indicate that summer *Hs* variability, like that in winter, is associated with the PDO, although at somewhat lower levels of correlation than in winter. Significant correlations with NINO3.4 are found for summer *Hs* mode 2 (the southwest-northeast dipole pattern). The summer *Hs* PCs are generally not well correlated with the atmospheric climate indices, except for PC3 with NP during the pre-1977 epoch. Weak or negligible correlation of *Hs* PCs with the atmospheric measures suggests that other factors are involved, i.e., more regional climate patterns than those represented by PNA and NP are affecting wave height variability.

4. Variability of H_S, T_P, and P_W Across the North Pacific

4.1. Spatial Distribution

[26] The patterns of *Hs*, *Tp*, and P_W at the 90th percentile level are useful to gage and interpret variations and trends

Table 1. Correlation of Mean Seasonal *Hs* PCs With Climate Indices[a]

	PDO			NINO3.4			-NP			PNA		
Mode	1	2	3	1	2	3	1	2	3	1	2	3
Winter (Nov to Mar): % Variance$_{1,2,3}$ = 45, 13, 10												
48–76	**0.65**	0.30	−0.28	**0.40**	**0.39**	−0.09	**0.54**	0.28	−0.14	**0.38**	0.31	−0.08
77–08	**0.39**	−0.02	0.16	**0.54**	0.14	**0.60**	**0.55**	−0.03	**0.41**	**0.63**	0.03	**0.38**
48–08	**0.65**	−0.03	−0.16	**0.48**	0.19	**0.28**	**0.62**	0.01	0.09	**0.60**	0.04	0.06
Summer (May to Sep): % Variance$_{1,2,3}$ = 26, 15, 9												
48–76	0.29	−0.11	0.13	0.05	**0.43**	0.13	0.20	−0.10	**0.42**	−0.10	−0.29	0.24
77–08	**0.48**	0.08	−0.35	0.22	**0.53**	−0.06	0.23	0.21	−0.02	0.15	0.10	0.04
48–08	**0.51**	−0.03	0.12	0.19	**0.48**	0.09	**0.25**	0.06	0.24	−0.01	−0.04	0.06
Full Year (all data): % Variance$_{1,2,3}$ = 30, 11, 10												
48–08	**0.43**	**0.20**	−0.03	**0.20**	0.08	**−0.10**	**0.44**	**0.10**	**−0.18**	**0.57**	0.03	**−0.29**

[a]Correlation coefficients, *r*, between the mean seasonal monthly anomaly principal components of modes 1, 2, and 3 (% variance given in subheadings) of *Hs* anomalies over the North Pacific north of 15°N with average winter and summer PDO, NINO3.4, -NP, and PNA indices of climate variability, with NINO3.4, effectively a substitute for the multivariate ENSO index (MEI). Correlations with *p*-values <= 0.05 are bold.

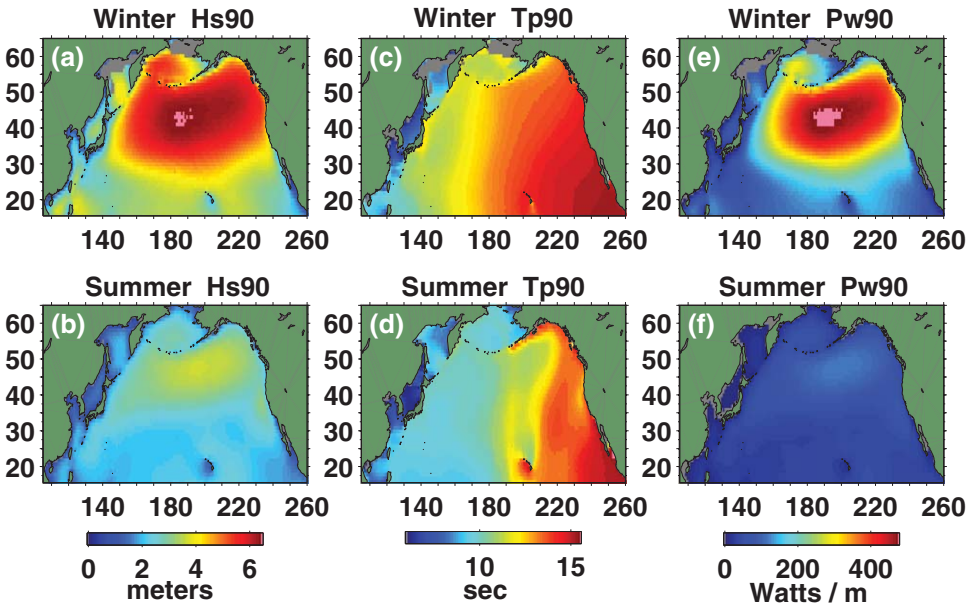

Figure 6. Distribution of 90th percentile *Hs*, *Tp*, and P_W during winter (top row, Nov.–Mar.), and summer (bottom row, May–Sep.) seasons.

of the higher extremes of these measures (Figure 6, 90th percentile; Hs_{90}, Tp_{90}, and Pw_{90}, respectively). The Hs_{90} pattern is similar to that determined by *Wang and Swail* [2001] over the 1958–1997 epoch. The maxima of both Hs_{90} and Pw_{90} are located in a zonal region north of about 35°N, resulting from intense storm activity associated with the Aleutian Low. Across the North Pacific, the peak in winter Pw_{90} spans about 20° of longitude (pink, Figure 6e), in contrast to the more localized peak in the winter Hs_{90} spatial pattern near the western end of the Pw_{90} peak zone. Zonal elongation of the peak Pw_{90} region results from the progressively higher *Tp* eastward along the apparent dominant wave height, and presumably wave generation region, in the core midlatitudes (35°N–50°N) across the North Pacific. Under intensifying storms as fetch expands and persistent winds increase in strength, wind energy is imparted to longer period waves, increasing *Hs* and shifting *Tp* to longer periods [*Pierson and Moskowitz*, 1964]. As waves propagate away from their generation region, the combination of dissipation of shorter period wave energy and dispersion results in a decrease in *Hs* while longer period waves become more dominant. Thus the period of the peak waves, represented by Tp_{90}, increases eastward, away from the dominant Aleutian generation region near 185–190°E. The shadowing effect of the Hawaiian Islands for waves propagating from the north is evident in Figure 6.

[27] In winter and summer, the spatial distributions of more extreme wave heights and wave power, characterized by the 98th percentile level (Supporting information Figure S5), are similar to their 90th percentile patterns in Figure 6, with maxima in Hs_{98} and Pw_{98} located close to those of the Hs_{90} near 180°E. The similarity of Pw_{90} patterns to that of Hs_{90} results from the dominance of the Hs^2 term in equation (1).

[28] In summer, peaks in both Hs_{90} and Pw_{90} (Figures 6b and 6f) are approximately colocated, about 5°–10° north and east of their winter locations (Figures 6b and 6f). The peak level in summer Hs_{90} is only about half that of winter peak levels, while, in contrast, summer Pw_{90} is less than a third of winter levels, resulting from smaller, less intense storms producing lower *Hs* and reduced long-period wave energy during summer months. The summer Tp_{90} pattern is influenced by both boreal and austral storm activity, with austral waves causing the pronounced Hawaiian Island shadow north of the islands and contributing to high Tp_{90} levels along the coasts of northern Mexico and in the Southern California bight during summer months (Figure 6d).

4.2. Winter and Summer Trends

[29] Long-period changes in winter and summer wave activity can be characterized by trends in seasonal mean *Hs*, *Tp*, and P_W. During winter, statistically significant upward trends in mean *Hs* and mean P_W (Figures 7a and 7e) are observed at most locations north of 25°N, with the exception of a meridional region from about 200°–220°E. This broad-scale increase in P_W reflects an increase in the NRA-1 westerly winds across midlatitudes, described later in regards to PDO changes, and also suggests that over the 1948–2008 time span there was an intensification of winter storm activity over much of the North Pacific. Trends in mean P_W in Figure 7e amount to increases during winter over the entire 60 year period of about 20% or more compared with mean P_{W50} levels (shown in Supporting information Figure S5) over open ocean and West Coast middle latitudes, further described in a regional analysis below (see also trends in Figure 12). The locations of strongest upward trends in winter *Hs* and winter P_W (Figures 7a and 7e) are both about 5°–10° south of the peaks in their climatological mean 90th percentile patterns (Figures 6a and 6e). Trends toward longer-period peak waves, increasing mean winter *Tp*, occur over most of the North Pacific (Figure 7c) and is consistent with increasing winter storm intensity. The *Hs* and P_W trend maps in Figure 7 indicate that the strongest increase in mean storm activity has occurred in

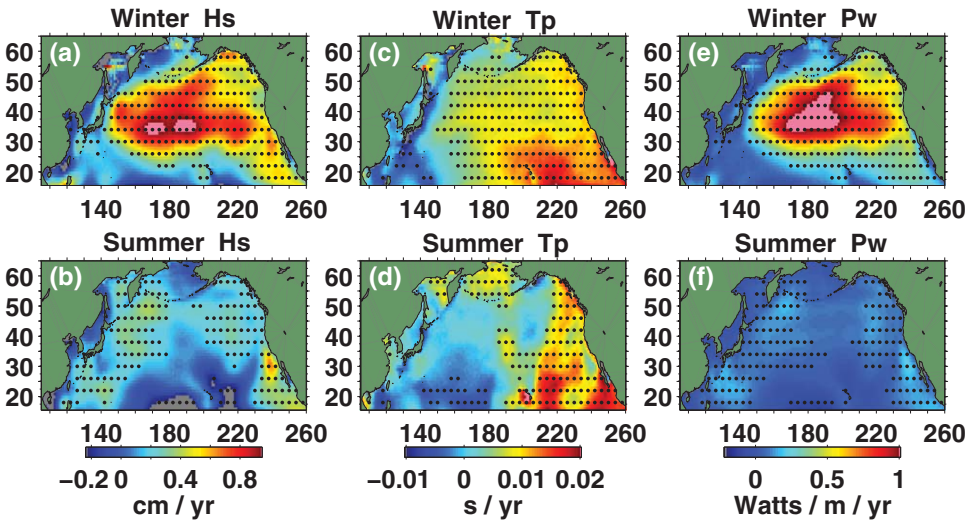

Figure 7. Seasonal trends in mean *Hs*, *Tp*, and P_W during winter (top; Nov.–Mar.) and summer (bottom; May–Sep.) seasons over the 1948–2008 epoch. Some regions gray (pink) either lack data or had trends less (greater) than the minimum (maximum) range indicated. Trends significantly different from zero at the 95% level at a minimum of 10 of 16 grid nodes in 4° × 4° (lat, long) regions are indicated by black dots centered within respective regions. The regional trend significance identification methodology applies to all subsequent similar figures.

the western North Pacific during winter. This is likely associated with the westward shift in the dominant mode-2 *Hs* EOF peak during the second half of the analysis period (compare Figures 5b and 5e). While the spatial patterns of trends in mean *Hs* and P_W are irregular, the upward trend tendency is strong over a zonal region centered near 37°N (Figures 7a and 7e), suggesting increased storm activity at lower midlatitudes during later epochs.

[30] The winter *Hs* trend pattern is generally consistent with increasing *Hs* in the boreal winter at higher latitudes and decreasing trends at more southerly latitudes [*Wang et al*., 2009].

[31] Particularly important from a societal perspective are the significant upward trends along the Pacific coast of North America. This long-duration WW3 model *Hs* trend appears to be consistent with upward trends in wave heights from shorter buoy wave records along the California coast [e.g., *Seymour*, 2011]. The relatively weak upward trend off the Washington-Oregon coast is consistent with the trend analysis of corrected buoy data by *Gemmrich et al*. [2011], with the lack of statistical significance likely due to either the much longer WW3 model data record used here than that available from buoy data, or the spatial characterization employed versus the buoy point measurements.

[32] During summer months, upward trends in both mean *Hs* and P_W have much lower magnitude (Figures 7b and 7f) and lack the broad spatial significance that is observed during winter across the central North Pacific, reflecting regionally variable smaller increases (or reduction) in summer storm intensity. However, although small, the trends are generally positive along the Pacific coast, indicating that even during summer months North Pacific storm activity has undergone regional increases.

[33] During summer, upward trends in mean *Hs* and *Pw* (Figure 7b) along the southern California coast suggest that northerly long-shore winds have intensified. Upward trends along the Mexican coast likely reflect increasing storm activity in the South Pacific and/or Southern Oceans, consistent with increasing northward-propagating long-period swell causing the upward trend in mean summer *Tp* south of the Hawaiian Islands (Figure 6d). Although wave amplitudes are generally relatively small during summer along the southern California coast (Figure 6b), these significant upward trends in *Hs* and *Tp* are beneficial for beach accretion [*Adams et al*., 2007]. Natural beach replenishment during summer months helps to buffer coastal infrastructure from initial winter wave activity and has great economic importance for California.

4.3. Hs_{90} Exceedance Distributions

[34] Variations and long-term increases in mean wave activity are an important indicator of a fluctuating wave climate, but changes in the occurrence of the higher-amplitude portion of the *Hs* distribution are more significant from a coastal impacts perspective. Seasonal trends were determined from all *Hs* and *Pw* occurrences above the 90th percentile level, Hs_{90T}, and Pw_{90T}, at each grid node during respective seasons. Trends in Hs_{90T} during winter months (November to March) (Figure 8a) exhibit a pattern similar to mean *Hs* seasonal trends (Figure 7a). Notable features in the winter Hs_{90T} (Figure 8a) pattern are the relatively strong increases in the central western North Pacific and along and offshore the California coast.

[35] The winter Pw_{90T} trend pattern is necessarily similar to Hs_{90T}, but the outstanding feature is the region of strong upward Pw_{90T} south of the Aleutians centered near 45°N, 200°E (Figure 8c). Importantly, although smaller, significant upward Pw_{90T} trends occur over much of the U.S. West Coast.

[36] During summer, the Hs_{90T} trends north of about 40°N are generally not significant (Figure 8c). However, summer mean *Hs* (Figure 7b) has significant, although weak, upward trends in this region, indicating that although

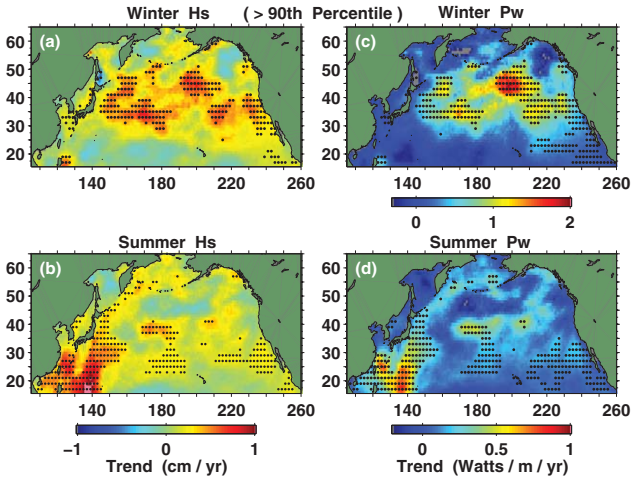

Figure 8. Trends of Hs_{90T} and Pw_{90T}, the means of *Hs* and *Pw* exceeding the 90th percentile level during winter (Nov.–Mar.; a and c), and summer (May–Sep.; b and d) seasons. Note that the range in Figure 8d is about half that in Figure 8c. Trends that pass the 95% significance test at a minimum of 3 of 4 grid nodes in 2° × 2° (lat, long) regions are indicated by dots. Scale in Figure 8b applies to Figure 8a.

the summer mean *Hs* is increasing, the highest wave activity, characterized by Hs_{90}, is not. In contrast, the southwestern Pacific shows significant strong upward Hs_{90T} and Pw_{90T} trends during summer (Figures 8b and 8d), possibly related to increasing strength of trade winds since the early 1990s [*Merrifield*, 2011]. These regional trends appear to be associated with the comparative strengthening of the *Hs* mode-3 EOF weights in that region during the 1978–2008 epoch (compare Figures 5c and 5f).

5. P_W Spatial and Temporal Patterns and Climate Associations

5.1. Spatial Patterns

[37] Wave power, P_W, depends on peak wave period, T_P, in addition to wave height, *Hs* (equation (1)). Because T_P depends on storm size, intensity, and duration, P_W variability more fully describes storm and wave energy changes. Thus, although the Hs^2 term dominates and consequently P_W EOF spatial patterns are expected to be similar to *Hs* EOF patterns (Figure 5), P_W EOFs give a better characterization of storm wave activity across the North Pacific, which is particularly relevant to the magnitude of wave impacts along coasts. Coastal relevance of P_W variability results partly because wave runup, the vertical height above a still water reference level reached by incident waves at the shore, increases with higher *Hs* and longer *Tp* [*Stockdon et al*., 2006].

[38] The dominant pattern of P_W variability across the North Pacific is characterized by mode-1 EOF centered in the mid-Pacific north of Hawaii at about 40°N, and extending to the Pacific coast of North America (Figure 9a). The first three P_W modes (Figures 9a–9c) account for 70% of the variance, as opposed to only about 50% accounted for by the first three *Hs* modes. P_W mode 1 over the entire WW3 record (1948–2008) has a spatial pattern that resembles *Hs* mode 1, but accounts for substantially more of the variance than *Hs* mode 1 (45% versus 30%, respectively) during either of the epochs or over the full record. The spatial patterns and variance for the three EOF modes for the full 1948–2008 *Hs* record (not shown) are similar to those of the 1978–2008 epoch in Figures 5d–5f, indicating that the latter epoch dominates the full record EOF spatial structures of both *Hs* and P_W.

[39] P_W EOF modes 2 and 3 (Figures 9b and 9c) resemble corresponding *Hs* modes (Figures 5b, 5e and 5c, 5f). The P_W mode-3 dipole has its dominant pole in the Aleutian Low region, likely associated with the effect of NP intensity on North Pacific wave energy. However, the coastward shift and expanded influence of the P_W mode-3 eastern pole (compare Figure 9c with *Hs* Figures 5c and 5f) likely has a stronger influence on coastal wave activity. All P_W modes shown in Figure 9 contribute to wave energy along much of the Pacific coast of North America, with the north-south mode-2 demarcation reflecting the approximate boundary near Cape Mendocino that separates generally higher (north) and lower (south) coastal wave energy [*Bromirski et al*., 2005].

5.2. Principal Components

[40] The monthly to multidecadal variability of wave power is indicated by the principal components (PCs) associated with P_W EOF modes (Figures 9d–9f). P_W mode-1 principal component (PC1) shows a significant increase in the occurrence of high-amplitude positive values after the mid-1970s regime shift, consistent with enhancement during the warm phase of the PDO. Additionally, as indicated by the 3 year running means, P_W PC1 roughly conforms to the PDO cool phase conditions prior to 1977, near 1990, and during the 2000s when a downward trend occurs. PC2 represents the north-south wave power anomaly dipole and straddles the major PDO and PNA core region in the North Pacific, and consequently is not strongly correlated with any of the selected modes of climate variability (Table 2). Prominent peaks for all three P_W modes during the very strong 1983 and 1998 El Niño's demonstrate a strong influence of ENSO-related forcing. The timing and placement within the WW3 record of P_W peaks from heightened storm activity under strong ENSO's strongly influences the magnitude of the upward trends determined.

5.3. P_W Climate Associations

[41] Climate associations with P_W were determined by correlating P_W PCs with the PDO, NINO3.4, NP, and PNA climate indices (Table 2). As would be expected, the highest correlations of P_W PC1 are with atmospheric circulation (sea level pressure (SLP) and geopotential height) indices NP and PNA, respectively, consistent with the strong association of U.S. West Coast wave energy with large-scale SLP patterns during winter months [*Bromirski et al*., 2005]. The significant increase in mode 2 and 3 correlations from the pre- to the post-1977 epoch indicates a stronger influence of ENSO on wave energy during the latter epoch under the warm phase of the PDO. The associated increase in correlations from pre- to post-1977 of P_W PC2 and PC3 with NP and PNA are consistent with teleconnections from

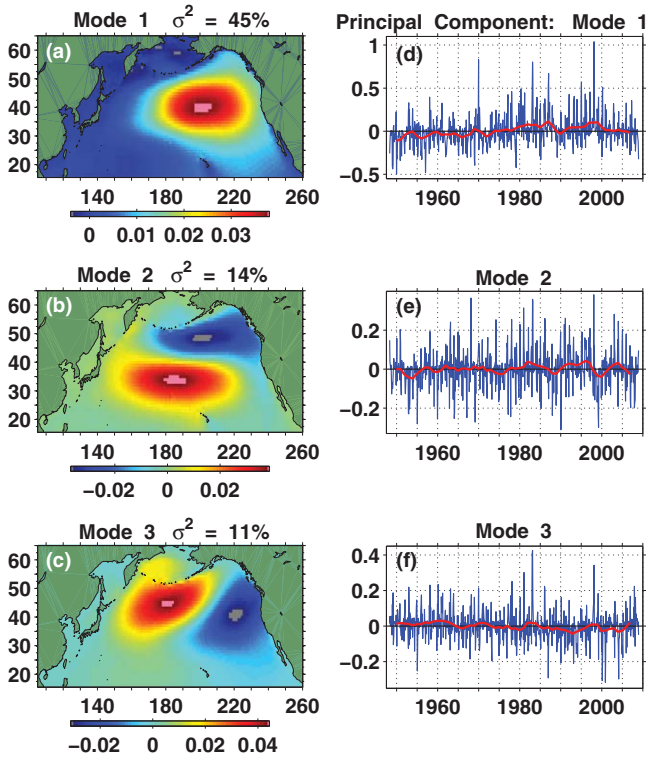

Figure 9. Spatial and temporal wave power, *Pw*, variability over the 1948–2008 time period described by (a–c) empirical orthogonal function (EOF) patterns and (d–f) associated principal components (PCs, with 3-yr running means (red lines)) for the first three modes. These were determined from monthly *Pw* anomalies (formed from the difference between the monthly mean and the climatological mean at each grid point) normalized to unit variance. Positive PC excursions are associated with the red spatial patterns. The variance, σ^2, accounted for by each mode is given in Figures 9a–9c.

the tropics having a stronger effect on midlatitude atmospheric circulation (and hence wind) patterns during the latter period. The post-1977 period was dominated by the strong Aleutian Low patterns, apparently supported by the coincidence of very large El Niño events in 1982–1983 and 1997–1998 during the warm phase of the PDO [*Gershunov and Barnett*, 1998].

6. Strong Wave Power Events (P_E)

6.1. Event Wave Power

[42] Wave activity and impacts along coasts is highly sensitive to storm track, which is closely tied to broad-scale atmospheric patterns and associated wind characteristics. Both T_P and wave event duration are important factors in estimating the potential for coastal impacts. Following *Bromirski and Kossin* [2008], the wave power per storm event, P_E, at each grid node is determined from

$$P_E = \int_0^\tau P_W dt \tag{2}$$

i.e., the integral of P_W over the wave event duration, τ; where P_W is given by equation (1) over an event. Because P_E results from both H_S and T_P wave parameters, P_E provides a better measure of the potential for severe coastal impacts from storm waves than H_S alone.

[43] Here wave events are defined as H_S being continuously above a proscribed threshold for at least 12 h. The 12 h requirement is important because the Pacific Coast of North America has a mixed-tide regime characterized by two usually unequal daily high tides and two unequal daily low tides, with the diurnal tide range generally increasing from south to north [*Flick et al.*, 2003]. Since the most extensive damage to coastal infrastructure occurs when high waves occur near high tide, the 12 h event criterion ensures that waves for these events will occur during a high tide, although potentially not during the highest diurnal level. These constraints on event identification allow characterization of changes in the incidence and spatial variability of strong storm-wave events that generally cause the greatest coastal and societal impacts. Since the WW3 model data outputs are 4 samples/d (every 6 h), three consecutive H_S estimates above threshold thus gives an effective τ for extreme events of at least 12 h. The 90th percentile threshold that was employed is explained below.

Table 2. Correlation of Mean Seasonal *Pw* PCs With Climate Indices[a]

	PDO			NINO3.4			-NP			PNA		
Mode	1	2	3	1	2	3	1	2	3	1	2	3
Winter (Nov to Mar): % Variance$_{1,2,3}$ = 46, 14, 11												
48–76	**0.75**	0.07	−0.03	**0.40**	0.22	0.03	**0.83**	−0.17	−0.24	**0.71**	0.01	−0.29
77–08	**0.50**	−0.31	−0.07	**0.50**	**−0.45**	**−0.45**	**0.78**	**−0.53**	**−0.41**	**0.75**	**−0.43**	**−0.44**
48–08	**0.72**	**−0.27**	0.12	**0.47**	−0.22	−0.22	**0.84**	**−0.46**	−0.19	**0.77**	**−0.32**	−0.23
Summer (May to Sep): % Variance$_{1,2,3}$ = 37, 12, 9												
48–76	0.33	−0.35	0.26	−0.09	**−0.48**	0.08	**0.41**	0.09	0.02	0.03	−0.06	**−0.44**
77–08	**0.40**	−0.15	0.27	0.18	−0.04	0.14	0.21	0.05	−0.07	0.23	0.10	−0.15
48–08	**0.47**	−0.15	**0.32**	0.13	−0.18	0.15	**0.28**	0.06	−0.04	0.11	0.03	**−0.28**
Full Year (all data): % Variance$_{1,2,3}$ = 45, 14, 11												
48–08	**0.40**	**−0.10**	**0.10**	**0.23**	**−0.11**	−0.06	**0.46**	**−0.15**	−0.03	**0.58**	**−0.13**	**−0.10**

[a]Correlation coefficients, *r*, between the mean seasonal monthly anomaly P_W principal components of modes 1, 2, and 3 (% variance given in subheadings) of *Pw* anomalies over the North Pacific north of 15°N with average winter and summer PDO, NINO3.4, -NP, and PNA indices of climate variability. Correlations with *p*-values <= 0.05 are bold.

[44] Coastal impacts from strong wave events during winter months depend on peak P_E and event duration, as well as the frequency of their occurrence. Given the dominance of the *Hs* term in equation (1), we expect that the patterns of both summer and winter P_E should be similar to strong *Hs* spatial patterns, with differences resulting from modulation of P_W by *Tp* and integration over τ.

6.2. Trends in P_E

[45] Changing climate patterns can have a significant impact on atmospheric circulation patterns that drive wave generation. Upward trends in wave amplitudes over the North Pacific reflect increasing cyclone frequency and intensity [*McCabe et al.*, 2001; *Graham and Diaz*, 2001; *Wang et al.*, 2006]. However, from a practical coastal impacts perspective, the number and strength of strong wave events that impact local coasts is more important than the number of North Pacific extratropical cyclones (ETCs), since a strong storm can generate more than one strong wave event because of variable storm wind intensity and direction as an ETC propagates across the basin, and storm track and storm characteristics determine which coastal region is most strongly impacted. Realizing that trend estimates determined here are derived from model data that have inherent uncertainties, identification of the regions where significant upward trends over 1948–2008 are observed likely has more meaning than the magnitude of associated trends, which if steep are unlikely to be sustained over an extended time period. Here, trends in storm event wave power, P_E, were determined from the time series formed from each year's seasonal mean of all P_E events at each grid point. Each event is defined by *Hs* exceeding both the seasonal (winter or summer) spatially variable Hs_{90} level, determined over the entire record at each grid node, for at least three consecutive realizations (12 h). The 12 h duration criterion also reduces the likelihood of inclusion of *Hs* transients resulting from short duration NRA-1 wind field inhomogeneities.

[46] The criterion for event identification has a strong influence on the spatial patterns of associated statistically significant P_E trends. For example, using an Hs_{98} threshold instead of the Hs_{90} threshold gives only a few isolated locations where trends exceeding this threshold (not shown) are statistically different from zero. Alternatively, for the Hs_{90} threshold, the substantial increase in the number of occurrences exceeding an Hs_{90} threshold gives a larger sample size while still including the most extreme realizations. This lower threshold yields significant Hs_{90T} trends over much of the North Pacific domain (Figures 8a and 8b), and allows a more thorough identification of overall changes in regional patterns of strong P_E events. Hs_{90} is thus the threshold that is employed in the event-scale analyses. However, examination of trends in extremes, i.e., the largest event in each season, is also presented.

6.2.1 Trends in Winter P_E

[47] The pattern of significant trends in winter P_E (Figure 10a) is similar to the winter Hs_{90T} pattern (Figure 8a), as expected, but the area where the trends are statistically significant is reduced considerably and is displaced to the east with a concentration offshore of California and Oregon. The strongest upward trends in winter P_E do not occur in the region of strongest Hs_{90} and P_{W90} trends in the western North Pacific (Figure 8), but rather over the eastern North Pacific between about 30°–45°N. These strong P_E trends are approximately colocated with the eastern pole of P_W mode 3 (Figure 9c), which along with P_W mode 2 has a strong ENSO connection during the post-1977 epoch (Table 2). The combination of these factors likely has a considerable influence on the strength of upward trends in this region. Storms and wave energy from these regions generally propagate eastward, resulting in upward trends in P_E along much of the Pacific coast of North America.

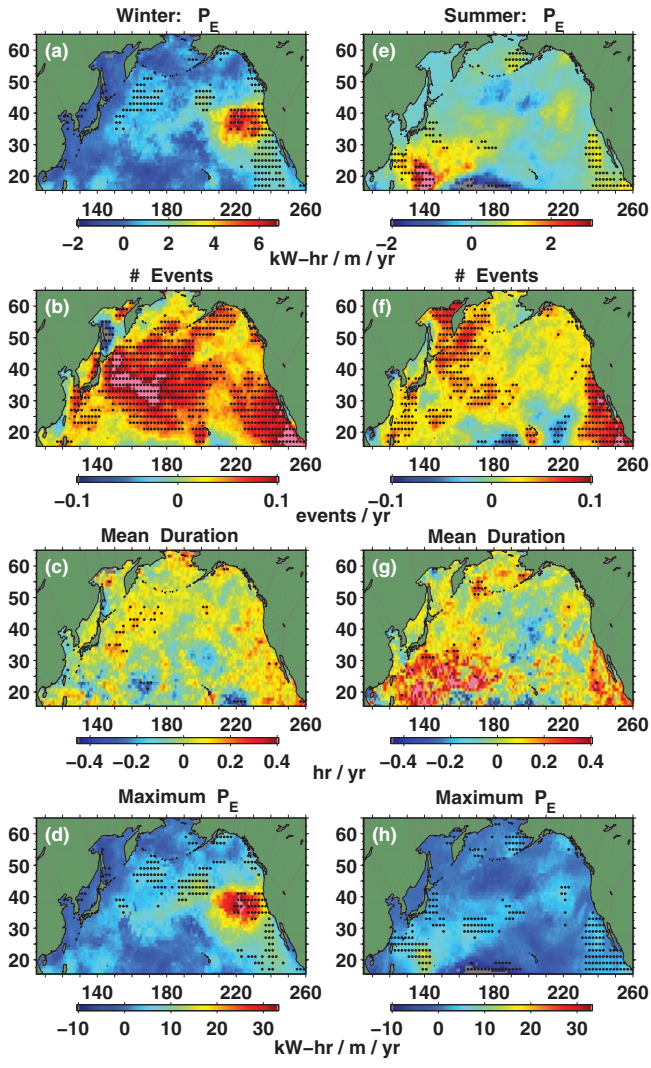

Figure 10. Trends in wave power event characteristics during winter (left panels, a–d) and summer (right panels, e–h) seasons over the model record (1948–2008) determined for all events during respective seasons. (bottom row) Trend in the maximum P_E event during each respective season. Events were defined at each grid node by *Hs* continuously exceeding the 90th percentile threshold at least three consecutive realizations (12 hr duration). Some regions in gray either lack data or had trends less than in gray (greater than; pink) the minimum (maximum) range indicated. Trends that pass 95% significance test over 2° × 2° (lat, long) regions, as in Figure 8, are indicated by dots.

[48] Another region with a significant upward trend in winter P_E is centered near [45°N, 200°E], probably a result of storm activity associated with ENSO-related southeastward displacement of the Aleutian Low [*Latif and Barnett*, 1996]. This high-activity region is likely an important influence on the locations of the dominant pole of the three P_W modes (Figure 9). The influence of ENSO on the location of the Aleutian Low is reflected in the strong correlations of NINO3.4 with winter P_W PCs (Table 2) during the latter epoch.

6.2.2. Trends in Summer P_E

[49] The pattern of summer (May-September) P_E trends (Figure 10e) is closely aligned with summer Hs_{90T} (Figure 8d). Summer trends are not statistically significant over much of the North Pacific. A major exception occurs in the southwestern North Pacific, which exhibits strong upward trends in the magnitude of wave events. Correspondingly, *Young et al*. [2011] found increasing wave height in this region from satellite altimetry, but over a much shorter record length. These increases, in a very different region from those that appear in winter, are consistent with the persistence of increasing trade wind and/or equatorial circulation-related wind forcing in this region [*Merrifield*, 2011].

[50] Although not as strong, a significant upward trend in summer P_E is also observed along the Southern California/Baja coast. The southward extension of this pattern suggests that it may be related to increased Southern Hemisphere swell, reflected in the summer Tp_{90} shadow north of the Hawaiian Islands and the peak in the Tp_{90} distribution along the Southern California/Baja coast (Figure 6d), as well as in the trend patterns for both summer *Hs* and *Tp* (Figures 7b and 7d).

6.2.3. Trends in the Number of Winter P_E Events

[51] In contrast to the changes in the *magnitude* of winter P_E events, which were concentrated in the eastern North Pacific, there was a much broader and western-displaced pattern of increase in the *number* of winter P_E events over 1948–2008. The increases are found across most of the western North Pacific, but less so eastward of 180°E. The steepest and most significant upward trends are in the central and western regions of the basin, and along the Baja/Mexican coasts (Figure 10b). The magnitude of the upward trends in these regions is approximately equivalent to one additional strong wave event each winter for each decade of the record. Comparison of Figures 10a and 10b indicates that significant upward trends in the magnitude of winter P_E events coincide with upward trends in the number of P_E events only over relatively small regions in the North Pacific.

6.2.4. Trends in the Number of Summer P_E Events

[52] The number of summer P_E events also increased in the central and western regions of the basin (Figure 10f), in general agreement with *Sasaki et al*. [2005]. Importantly, significant upward trends in the number of summer P_E events occur along most of the U.S. Pacific coast, with the steepest upward trends off the southern California/Baja coasts. Increasing numbers of summer P_E events in this coastal region may be partly the result of increasing storm activity in the Southern Ocean and the South Pacific during the austral winter, with the importance of southern wave activity evidenced by the Hawaiian Island T_P shadow (Figure 6d) and the distribution of summer mean T_P (Figure 7d). The upward trend in the number of summer P_E events in this coastal region has important implications for enhanced beach accretion during summer months.

6.2.5. Trends in Mean Duration of P_E Events

[53] Changes in the mean duration of P_E events were determined from the mean of all events during all respective seasons. In general, winter mean P_E duration increased over most of the North Pacific basin (Figure 10c), but except at isolated locations west of Baja Mexico, these increases failed to qualify as statistically significant. During summer, significant upward trends in summer mean P_E duration occurred over isolated locations in the southwestern North Pacific (Figure 10g), evidently associated with increasing summer wave intensity there.

6.2.6. Trends in Yearly Maximum P_E, Winter Season

[54] Increases in extratropical cyclone (ETC) intensity and associated extreme wave heights have been identified across the North Pacific [*Wang and Swail*, 2001; *Graham and Diaz*, 2001; *Wang et al*., 2006; *Seymour*, 2011], with the greatest increases concentrated in the mid-to-high latitudes. The increasing trends in ETC intensity in these regions are likely to result in increasing extreme P_E, which can be described spatially by trends in the maximum wave power event, P_{Emax}, at each grid node in each winter.

[55] As would be expected, regions having the strongest upward trends in winter P_{Emax} (Figure 10d) are closely colocated with regions where winter P_E showed an increase (compare Figure 10d with Figure 10a). Most notable from a coastal impacts perspective are the significant upward trends in winter P_{Emax} along the central California and Vancouver, BC coasts, although notably not along the Oregon-Washington coasts. The significant upward trends in P_{Emax} over the eastern midlatitudes and along the West Coast (Figure 10d) occur in conjunction with generally no significant change in the occurrence and mean duration of events in these regions (Figures 10b and 10c).

6.2.7. Trends in Yearly Maximum P_E, Summer Season

[56] As for winter P_{Emax} trends, the summer P_{Emax} trend pattern (Figure 10h) is similar to summer P_E (Figure 10e), with significant upward trends in the western Pacific and along the southern California/Baja coasts. The increasing summer wave intensity along the southern California coast likely facilitates beach accretion, potentially reducing the impact of at least initial winter storm wave impacts, particularly at beaches near their equilibrium position.

7. Regional Variability and Associations

[57] Changes in wave energy in specific regions of the North Pacific, such as along the Pacific coast of North America, depend on the configuration of broad-scale atmospheric circulation patterns that determine storm characteristics, including wind patterns, wind strength, and storm track. The portion of the coast most strongly impacted by intense wave activity is largely determined by the location of the dominant wave generation region. More intense storm activity closer to the coast will generally have greater impact at nearest coastlines. For example, wave activity that is concentrated at more northerly locations relatively near the coast (i.e., north of 45°N and east

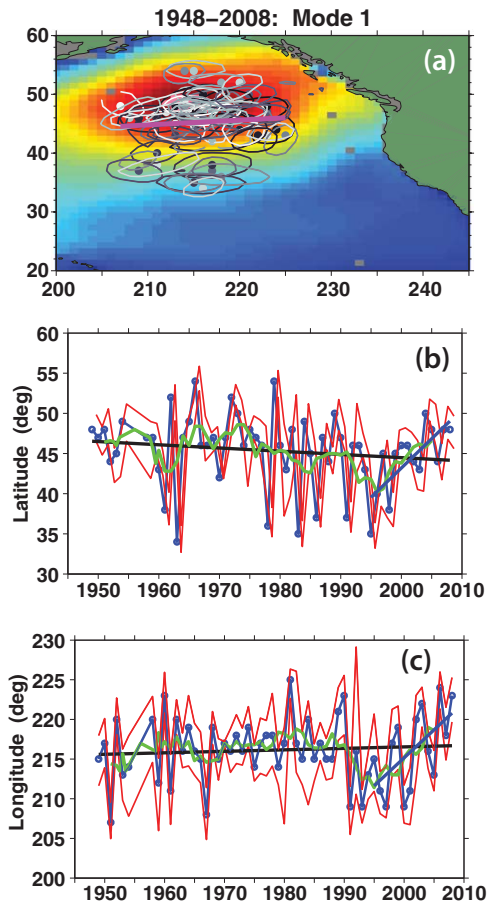

Figure 11. Variability of the dominant location of wave heights over the eastern North Pacific during winter (Nov.–Mar.). (a) Representative EOF spatial pattern of winter *Hs* (Nov.Mar.) over 1948–49. Successive winter peaks in mode 1 EOFs (dots) and their associated 98th percentile contours are color-coded by year (light-to-dark). The least squares trend line of the longitudinally-ordered EOF peaks (magenta line) gives an estimate of the central tendency of peak wave locations. (b) Latitude of the EOF peak (connected blue dots) and the range of their respective north-south 98th percentile extent (red lines), with the least squares trend (black line) and 5 yr running mean (green line) also shown. (c) Same as Figure 11b, except for longitude, with east-west extent shown instead. Least squares trend since 1992 (blue lines).

of 200°E) will generally have greater impact north of Cape Mendocino than at more southerly coastal locations.

7.1. Dominant Eastern North Pacific Winter Wave Generation Locations

[58] Identification of a systematic change in the location of the dominant winter wave region is key to explaining patterns of coastal impacts [*Bromirski et al*., 2012; *Graham*, 2005; *Storlazzi and Griggs*, 2000]. We expect the wave generation region to be characterized by strong, repeated variation of *Hs* on synoptic time scales, whose dominant location can be identified using a within-winter EOF analysis of synoptic variability. Thus, variability of the dominant wave generation region location in the eastern North Pacific during winter (November-March) was investigated using a series, one set for each winter, of empirical orthogonal functions (EOFs) calculated from the 6 h *Hs* fields over the region bounded by 20°–60°N and 200°–250°E (Figure 11). The spatial pattern in Figure 11 is a color coded, from cool-to-warm, map of weightings low-to-high, respectfully, of the EOF mode 1(computed over the 1948–1949 winter) of the 1949–2008 series. The sequence of locations of the peak of EOF 1 provides a measure of how the dominant winter *Hs* variability changes over the record. Winter *Hs* mode 1 typically accounts for 40% or more of the *Hs* variance over the region, with mode 2 less than half that. The proximity of the wave generation region to the West Coast of the United States affects both wave amplitude and incident wave direction.

[59] Figures 11a–11c reveal substantial north-south and east-west excursions of the location of peak winter *Hs* over the eastern North Pacific. Winters with easterly shifted centers of peak wave activity have greater impacts along the Pacific Coast, and those whose centers are shifted southward and eastward have greater impacts along the California coast. As a rule, the major pattern of synoptic time scale wave variability is concentrated north of 40°N and west of 225°E, although there are years when peak activity is shifted southward, e.g., occasional years from 1950 through the early 1970s, and a more concentrated sequence of years during the mid-to-late 1990s, with a general tendency for more southerly wave activity during El Niño.

[60] Latitude and longitude locations of the EOF mode-1 peaks (Figures 11b and 11c) show the north-south and east-west extents of dominant wave activity for each winter. Trend lines indicate any consistent shift in the mean latitude and longitude of peak wave activity that may have taken place over 1948–2008 time period. The spatial distribution of winter peak *Hs* locations (Figure 11a) is accompanied by a tendency for decreasing latitude (southward trend) over the latter half of the 20th century (Figure 11b, black line). There is considerable variability at time scales shorter than the long-period trends, however. Since about 1995, winter 5 year running means (Figures 11b and 11c; green curves) exhibit a northeastward shift in the dominant centers of wave activity, indicated by least squares trends (Figures 11b and 11c; thick blue lines). This recent shift toward heightened Northeast Pacific wave activity is consistent with the upward trend in *Hs* off the Washington-Oregon coast determined from unadjusted NOAA eastern North Pacific wave buoy records [*Ruggiero et al*., 2010; *Seymour* 2011], with *Gemmrich et al*. [2011] obtaining a lower *Hs* increase determined at NOAA buoy 46005 (46.083°N, 229.0°E) after adjusting for instrument changes. The northeast shift in peak wave power seen here also appears to be consistent with the shift in the proximity of the *Hs* mode-2 northern pole nearer the coast (Figure 5), in conjunction with enhanced contributions from *Hs* mode 1. More northerly centers of peak wave activity would likely diminish extreme wave activity along the California coast south of Cape Mendocino, and hence reduce the occurrence of coastal flooding events in that region.

7.2. Regional Variability and Trends in Wave Power Anomalies

[61] To further describe anomalous North Pacific wave activity, variability of P_W was investigated in a set of key

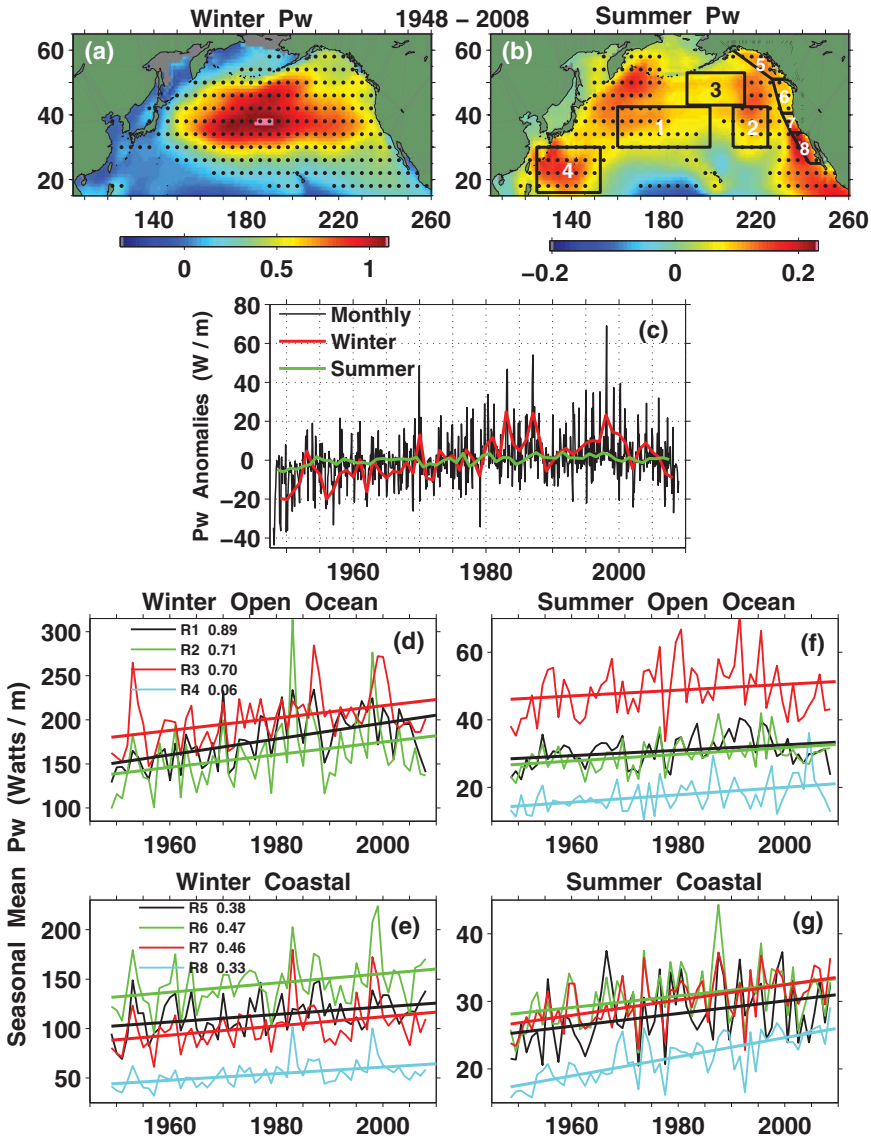

Figure 12. Seasonal variability and trends in anomalous wave power across the North Pacific 1948–2008 during (a) winter (Nov.–Mar.) and (b) summer (May–Sep.) months (note different trend scales in Figures 12a and 12b, selected to enhance seasonal trends), with averages over the entire domain (c). Trends over 4° × 4° boxes in Figures 12a and 12b that are significantly different from zero at the 95th level, as in Figure 7, are indicated by dots. Regional (averaged over boxes delineated in Figure 12b) mean wave power during winter over (d) open-ocean and (e) coastal regions, and during summer (f, g) (see legends). Associated mean winter wave power anomaly trends (W/m/yr) are shown in Figure 12d and (e), with summer trends in (f, g) less than 0.14 W/m/yr. The R4 curve in Figure 12d, (not shown; mean = 42.7 W/m/yr), is not statistically significant from zero and has much lower variance than the other regions. (f, g) Same as Figures 12d and 12e except for summer months. Note that vertical scales differ significantly.

regions across the basin. As background, over the period of record from 1948 to 2008, annual P_W averaged across the North Pacific north of 15°N increased about 12% (Figure 12), presumably reflecting changes that occurred in association with the mid-1970s regime shift. The bulk of this increase can be attributed to increases of P_W in winter (which exhibited a 15.5% increase) when the mean wave power is high, as opposed to summer (which shows an increase of 8%) when the mean power is low. Changes in anomalous P_W are useful in describing and interpreting climate variability and possible changes in storm patterns. Monthly P_W anomalies were determined as the difference between the monthly mean and long-term climatological mean at each grid point. The pattern of anomalous monthly winter P_W trends (Figure 12a) is similar to that of mean winter *Hs* and P_W trends (Figures 7a and 7e), resulting from the dominance of high-amplitude *Hs* during winter months on seasonal P_W estimates. Upward trends in summer anomalous P_W (Figure 12b) also track mean summer *Hs* and P_W trends (Figures 7b and 7f). Of note is

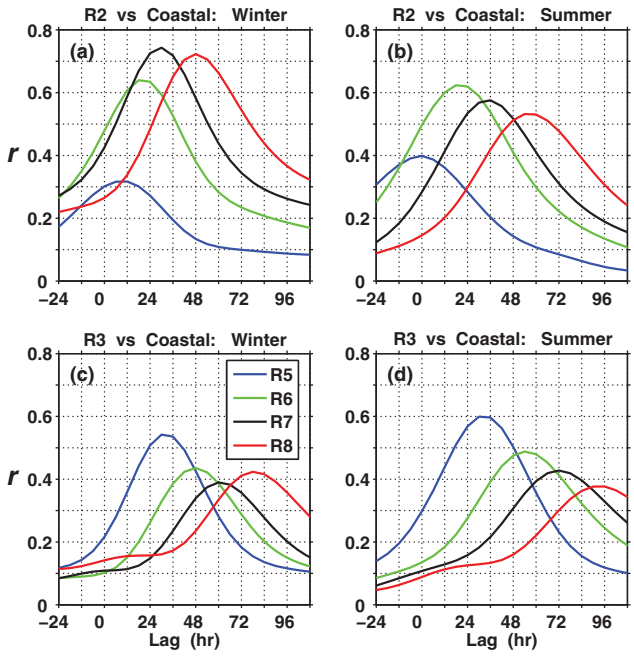

Figure 13. Mean wave power correlation between regions. Cross correlations, *r*, for mean winter (Nov.–Mar) mode 1 principal component P_W anomalies over regions R2 and R3 (see Figure 12) versus those at coastal regions R5–R8. Peak correlations at positive (negative) lags imply R2 or R3 lead (trail) wave arrivals at R5–R8, with positive lags consistent with wave propagation from R2 and R3 to the coast. Legend in Figure 13c applies to all panels.

the comparatively steep upward trend off the southern California coast during summer.

[62] Monthly P_W anomalies averaged over the entire North Pacific basin (Figure 12c) show peaks that correspond to P_W PC1 (Figure 9a), and reflect the general increase in anomalous P_W that occurred after the mid-1970s regime shift. Increased P_W over the basin is dominated by winter wave activity, with extreme basin-wide anomalous P_W primarily occurring during strong ENSO episodes. The influence of the PDO is evident by generally elevated anomalous P_W during the PDO warm phase, and of lower P_W during the cool phase, in particular before the mid-1970s regime shift and also during the short-duration cool phase near 1990. Importantly, the shift toward lower North Pacific wave power after 2000, manifested by a downward trend in anomalous P_W that is somewhat more pronounced than that observed for P_W PC1 in Figure 5d, appears associated with a recent shift of the PDO to its cool phase [*Bromirski et al*., 2011] (see http://jisao.washington.edu/pdo/).

[63] Eight ocean regions (boxes in Figure 12b) were selected based on observed wave variability [*Bromirski et al*., 2005] and P_W variability described in Figures 7, 8, and 10, and important coastal regions. Wave power variability in open-ocean regions R2 and R3 likely has a close association with particular Pacific coastal regions defined as: (R5) Gulf of Alaska/British Columbia, (R6) from Vancouver south to Cape Mendocino, (R7) Cape Mendocino to Pt. Conception, and (R8) Pt. Conception south to the Baja coast. Region R4 represents the subtropical portion of the far western North Pacific.

[64] All open-ocean regions show significant upward trends during winter (Figure 12d), with the exception of R4 (not plotted). Northernmost open-ocean R3 generally has the highest mean anomalous winter P_W, indicating that increasing storm intensity is more common at higher latitudes. Substantial winter interannual variability is observed over most regions, but is less at the most southern (R4 and R8) regions. During winter, relative amplitudes of mean anomalous P_W over R2 and R3 (Figure 12d) and R6 and R7 (Figure 12e) are consistent with more southerly storm tracks during the 1982–1983 El Niño winter compared to 1997–1998. Interestingly, the region R1 does not exhibit as strong an ENSO signal as R2 and R3, suggesting that the ENSO effect on P_W is more dominant in the eastern North Pacific.

[65] During summer (Figures 12f and 12g), R3 has the highest anomalous P_W activity, consistent with the location of the peak in summer P_W north of 45°N (Figure 6f). Most notable is the steep upward trend in anomalous P_W over R8, which is conducive for beach accretion along the California coast. This upward trend is likely partly due to increased wave energy from the Southern Hemisphere, as suggested by upward trends in summer P_W (Figure 7f) in that region.

7.3. Associations of Eastern Pacific Open-Ocean and Coastal Variability

[66] The location of open-ocean *Hs* and P_W peak activity has a strong influence on near-coastal wave direction, and therefore their transformation from deep water to the shore [*O'Reilly and Guza*, 1991]. Correlations of mean anomalous P_W mode-1 principal components (PCs) over R2 and R3 with the coastal region PCs confirm that open-ocean wave power leads activity at coastal regions, albeit with somewhat mixed relationships during winter months (Figures 13a and 13c). The correlations appear to reflect a more complicated winter extratropical cyclone pattern than indicated by the more consistent relationships during summer (Figures 13b and 13d). In winter, British Columbia southward to California coastal regions R6–R8 are more strongly correlated with R2 than R3, indicating that R2 is the more dominant wave source region, which is consistent with winter P_E trend patterns (Figure 10) and winter P_W anomaly trends (Figure 12a). Lags associated with peak correlation coefficient, *r*, affirm that R2 is the dominant winter open-ocean source region. The Alaska-British Columbia, farthest-north coastal region R5 is better correlated with R3 than R2, as would be expected given R5's proximity to R3.

[67] In association with region R2 during summer months, the shortest time lag for peak regional correlations (Figure 13b) is for coastal region R5, with successively longer peak correlation lags for coastal regions R6, R7, and R8. This lag sequence suggests that the dominant source region is farther north during summer months, likely near the northern boundary of R2. The northward shift of wave activity from winter to summer is consistent with the relative location of Pw_{90} winter and summer distribution peaks (Figures 6e and 6f, respectively). Analogous peak correlation time lags for open-ocean region R3 with the coastal regions (Figure 13d) show a consistent pattern indicative of north-to-south wave propagation. The higher correlations

Table 3. Correlation of Regional Mean P_W Anomalies With Climate Indices[a]

	MEI	NINO3.4	PDO	-NP	PNA
R1	**0.51** (69.8)	**0.42**	**0.74**	**0.85**	**0.73**
R2	**0.60** (89.1)	**0.53**	**0.60**	**0.80**	**0.76**
R3	**0.31** (79.6)	0.23	**0.55**	**0.54**	**0.54**
R4	**−0.26** (62.8)	**−0.33**	−0.05	−0.12	−0.21
R5	**0.25** (86.5)	0.23	**0.50**	**0.49**	**0.52**
R6	**0.28** (91.3)	0.24	**0.35**	**0.46**	**0.46**
R7	**0.46** (96.3)	**0.41**	**0.47**	**0.61**	**0.57**
R8	**0.56** (96.3)	**0.50**	**0.56**	**0.70**	**0.65**

[a]Correlation coefficients, r, between principal component mode 1 of mean winter (Nov to Mar) monthly P_W anomalies over regions R1 to R8 (see Figure 12) with average winter MEI, NINO3.4, PDO, -NP, and PNA indices of climate variability. Correlations with p-values <= 0.05 in bold. Percent variance explained by mode 1 PC's over respective regions is given in parentheses under the MEI r-values.

of R3 versus the coastal regions during summer compared to winter indicate that R3 provides a somewhat greater contribution to P_W along the coast during summer.

7.4. Association Between Regional P_W and Climate Patterns

[68] For storm impacts preparedness, it is useful for coastal managers to be able to anticipate winter wave power intensity levels, given that regional P_W variability may be related to particular patterns of climate variability. Similar to regional correlations (Figure 13), high monthly *Hs* variability across the North Pacific makes seasonal correlations more useful to anticipate winter coastal P_W intensity. A separate set of EOFs was constructed for the P_W anomalies in each of the eight regions. Relationships of P_W with climate variability were investigated by correlation of winter climate indices with winter (November to March) mode-1 principal components (PCs) for each of the regions. PC1 represents the dominant wave variability across the region. The P_W data were normalized to unit variance prior to PC determination. Winter averages of PCs and the climate indices were formed for use in the correlation analysis. The percent of the variance captured by the first EOF mode for each of the regions varies from about 41% (R1) to 85% (R7), with the size of the region exerting some influence (Table 3).

[69] Because the dominant region of winter North Pacific P_W variation (Figure 6e) lies within the domain that defines the NP index, it is not surprising that NP exhibits relatively strong correlations with the PC time series from most of the eight regions (all except R4, in the far western subtropics). As with the other climate indices, most of the significant correlations with NP are found with the mode-1 PCs of winter P_W anomalies (Table 3). Teleconnections from the tropics associated with ENSO [*Wallace and Gutzler*, 1981] result in strong correlations over most of the regions with MEI, and more southern regions with NINO3.4, demonstrating the influence of ENSO on atmospheric circulation patterns over the North Pacific. The significant correlations with the PDO are similar to those with NP and are consistent with previous results (Tables 1 and 2), indicating that stronger North Pacific storms are more common during the warm phase of the PDO. However, strong correlations with both MEI and NP suggest that both of these modes of variability have a significant effect on storm intensity across the North Pacific. The similar correlations with PDO suggest that the wave variability and the PDO may be covarying elements of a basin-scale response to strong atmospheric circulation patterns associated with both NP and ENSO. Note that the southwestern North Pacific region R4 is correlated, modestly, with the PDO, but with opposite sign, which is consistent with the PDO pattern across the North Pacific [*Mantua et al.*, 1997; *Bromirski et al.*, 2011]. The anticorrelation of R4 with MEI and NINO3.4 is also consistent with the lesser influence of winter wind intensity on P_W trends, compared to summer months, in that region. The fact that R4 is poorly correlated with NP and PNA is consistent with those higher midlatitude climate modes having little association with atmospheric variability in the southwestern North Pacific.

[70] Correlations of mean summer (May-September) mode-1 PC P_W anomalies over R1–R8 with the summer mean climate indices (not shown) are neither well

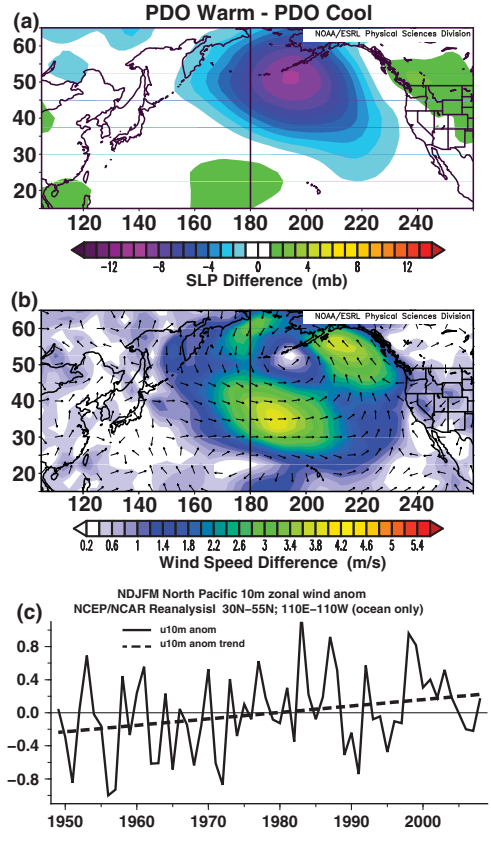

Figure 14. Winter (Nov.–Mar.) sea level pressure and wind over the North Pacific since 1948. Differences between mean (a) sea level pressure and (b) wind speed for the ten warmest (1987, 2003, 1984, 1988, 1998, 1977, 1994, 1986, 1985, 1970) versus the ten coolest (1956, 1972, 1962, 1991, 1950, 1951, 1976, 2012, 1971, 2009) PDO cases (i.e. warm – cool PDO). (c) Winter mean zonal 10 m wind speed over the dominant wave generation region from 30°N–55°N and 110°E–250°E (solid), with the least squares fit (dashed) significantly different from zero at the 95% level.

correlated nor significant, with the exception of the MEI with R4 ($r = 0.37$). This relationship over R4 suggests that ENSO-related factors may be influencing atmospheric circulation regimes that affect trade wind strength, resulting in increasing P_W in the western Pacific during summer months.

8. Discussion

[71] The WW3 simulation indicates that the North Pacific wave height and wave power, P_W, have considerable variability that is associated with the PDO over interdecadal time scales. The WW3 seasonal wave power variability and associated storm activity links with the PDO are supported by comparison of SLP and near-surface wind across the North Pacific (Figure 14) during the warm (positive) and cool (negative) phases of the PDO. The composite November through March SLP shows a deep Aleutian Low (Figure 14a), indicative of more intense storm activity over the North Pacific. The vector wind and wind speed difference between the same composite PDO winters (Figure 14b) shows the strongest wind vectors over the central Pacific, directed toward the region in the eastern Pacific where the greatest upward P_E trends are observed (Figures 10a and 10d). This pattern of wind variability is consistent with the PDO correlations in Tables 1–3 and heightened wave activity during the positive (warm) phase of the PDO. Consistent with this midlatitude intensification is the upward trend in zonal wind anomalies across the North Pacific over 30°N–55°N (Figure 14c), providing the basis for the upward trends in P_E off the California coast (Figures 10a and 10d).

[72] The association with the PDO is also emphasized by lower wave heights and P_W during the short excursion of the PDO to its cool phase near 1990 and a downward trend post-2000 after the recent cool phase shift (Figures 9d and 12c). P_W levels during these periods are comparable to those prior to the mid-1970s regime shift, suggesting that (1) assimilation of satellite data in the NCEP reanalysis winds beginning in the late 1970s has not introduced an appreciable upward bias in wind speed, as a wind speed upward bias should produce consistently elevated levels in P_W, and (2) if inhomogeneities are present, their impact does not strongly affect the associations with climate patterns. In other words, owing to the known changes in atmospheric circulation associated with the development of the warm phase of PDO and the massive ENSO events in 1982–1983 and 1997–1998, much of the P_W trends determined in this study appear to be driven by the time sequence of interdecadal and interannual variation rather than spurious changes from observational methodology. The PDO-related atmospheric decadal variability is apparently modulating storm systems.

[73] Critical to societal impacts is the timing of extreme P_E arrivals with high tide. Coastal locations where an upward trend in winter P_E occurs are expected to be subject to greater impacts from storm waves. Each of the extreme P_E events identified (Figure 10d) persists a "minimum" of 12 h, so each of these events along the Pacific coast must coincide with at least one of the tidal peaks, but the highest tide will not necessarily coincide with each extreme wave event. However, if the number of extreme events also increases, then it is likely that the coincidence of peak high tide with extreme P_E will also increase. Notably, where the steepest upward trends in winter P_E occur along the California coast (Figures 10a and 10d), neither the number of events nor the P_E mean duration exhibits a significant upward trend (Figures 10b and 10c). The U.S. Pacific coast adjacent to the strong upward trends in P_E and P_{Emax} is subject to impacts from these events. Correlations of the winter mean of these storm event descriptors over the region of steepest upward trends in Figure 10 with climate indices (Table 4) confirm that wave events in the active region are favored to be stronger, more frequent during El Nino, with the number of strong events modestly associated with all modes of climate variability. In contrast in the western North Pacific, although the number of winter events has increased, their intensity, as characterized by P_E trends, generally has not. In summer, all measures of P_E variability show significant upward trends in the southwest North Pacific.

Table 4. Correlation of Regional P_E Variability With Climate Indices[a]

	MEI	NINO3.4	PDO	-NP	PNA
P_E	0.24	0.25	0.21	0.21	0.17
P_{Emax}	**0.45**	**0.44**	**0.26**	**0.27**	0.25
Events	**0.39**	**0.33**	**0.35**	**0.31**	**0.41**
Duration	**0.30**	**0.31**	0.19	**0.28**	0.22

[a]Correlation coefficients, r, between the mean of winter (Nov to Mar) P_E, P_{Emax}, number of events, and mean duration over the region of maximum P_{Emax} increases bounded by 217.5°E–242.5°E and 33°N–42°N versus average winter MEI, NINO3.4, PDO, -NP, and PNA indices of climate variability (see Figure 10). Correlations with p-values <= 0.05 in bold.

[74] Coastal flooding and associated societal impacts are directly associated with regional mean sea level [*Bromirski et al.*, 2012]. For example, during the 1982–1983 El Niño winter, sea level along much U.S. Pacific coast rose by 15–20 cm during winter months, equivalent to global mean sea level rise over the entire 20th century [*IPCC*, 2007]. This was accompanied by extreme wave heights (and P_W levels) and storm surge [*Bromirski et al.*, 2003; *Bromirski and Flick*, 2008] along the California coast. Because extreme storm surge and waves are superimposed on regional sea level, and because extreme waves generally coincide with extreme surge [*Cayan et al.*, 2008], these factors contributed to the most severe flooding and destruction of coastal assets during the 20th century [*Storlazzi and Griggs*, 2000]. The 1982–1983 ENSO-episode represents the coastal impacts that will occur more frequently under rising sea levels, especially if the upward trend in extreme P_E along the California coast persists.

9. Summary and Conclusions

[75] A WW3 hindcast (1948–2008) provides a better understanding of wave height and wave power variability and estimates of underlying trends than widely separated short-duration buoy records. The WW3 open-ocean wave variability has good fidelity with North Pacific open-ocean buoy records, and to some extent with coastal buoy records. Furthermore, the WW3 variability is reasonably consistent

in its relationship to large-scale climate measures during the period before and after the Pacific climate shift in the mid-1970s. To better understand wave characteristics and their potential impacts, this study not only investigates significant wave height, *Hs*, but also wave power, P_W, which increases nonlinearly with *Hs* and is proportional to *Tp*.

[76] The WW3 simulation shows a general increase in *Hs* and *Pw* over most of the North Pacific. Fluctuations in winter wave *Hs*, *Pw*, and seasonal aggregates of high wave events have strong to moderate connections to the Aleutian Low, PDO, and ENSO. Elevated wave intensity is more common during the warm phase of the PDO, and during the warm phase of ENSO. Averaged over the North Pacific (north of 15°N), mean winter wave power, compared with mean pre-1977 PDO cool phase levels, increased by about 15% during the PDO warm phase from 1980 to 2000 (the increase is biased low due to the short duration cool phase excursion during 1989), with peak winter-wave levels about 30% greater. The placement in time of these PDO-related fluctuations has a strong influence on the upward trends that have resulted.

[77] Upward trends in the *number* of strong wave power events (P_E) have been quite broad scale, with changes exceeding one event per year per decade that are especially pronounced in the western North Pacific. In contrast to the broad pattern of increase in the number of strong events and the increases in Hs_{90} or Pw_{90}, the pattern of change in strong event *magnitude* has been more confined, with steepest winter P_E increases in a region close to the Pacific coast. The duration of strong P_E events has generally not increased over the North Pacific. In summer, all measures of P_E variability show significant upward trends in the southwestern North Pacific. Upward trends in summer P_E found along the southern California coast should enhance beach accretion there during summer months, which helps to buffer coastal infrastructure from at least the initial winter wave activity, and has great economic importance for California.

[78] Although the entire 1948–2008 record shows upward trends in *Pw* over the North Pacific basin, since about 2000 there has been a reversal. This recent decline in basin-wide *Pw* levels is consistent with lower wave activity during the cool phase of the PDO. Basin-wide *Pw* may remain subdued as long as the cool phase persists, which may eventually reduce or negate the upward trends seen over the 1948–2008 epoch. The magnitude and sign of the trends described are highly influenced by the timing of particular patterns of interannual and longer-term fluctuations, e.g., by the phase of the PDO and the timing of strong El Niño's.

[79] It is emphasized that these trends should not be considered to be a prediction of future changes because they are strongly influenced by natural variability that is characteristic of North Pacific climate. However, if upward trends in extreme winter wave event intensity continue, or if higher wave activity returns in the future when the PDO reverts to the warm phase, severe coastal impacts from flooding and erosion will increase. Coastal impacts, that result when high waves occur near peak high tides, will be exacerbated if (more likely when) regional sea level rise along the eastern boundary of the North Pacific resumes.

[80] **Acknowledgments.** Support for this study is gratefully acknowledged from NOAA through grant NA10OAR4310121 and the California Department of Parks and Recreation, Division of Boating and Waterways under contract 11-106-107 with SIO, as is support for DRC from the California Energy Commission and the NOAA RISA program. Comments from Dick Seymour are much appreciated.

References

Adams, P. N., D. L. Inman, and N. E. Graham (2007), Southern California deep-water wave climate: Characterization and application to coastal processes, *J. Coastal Res.*, *24*(4), 1022–1035.

Bromirski, P. D., and R. E. Flick (2008), Storm surge in the San Francisco Bay/Delta and nearby coastal locations, *Shore Beach*, *76*(3), 29–37.

Bromirski, P. D., and J. P. Kossin (2008), Increasing hurricane wave power along the U.S. Atlantic and Gulf Coasts, *J. Geophys. Res.*, *113*, C07012, doi:10.1029/2007JC004706.

Bromirski, P. D., R. E. Flick, and D. R. Cayan (2003), Storminess variability along the California coast: 1858–2000, *J. Clim.*, *16*(6), 982–993.

Bromirski, P. D., D. R. Cayan, and R. E. Flick (2005), Wave spectral energy variability in the northeast Pacific, *J. Geophys. Res.*, *110*, C03005, doi:10.1029/2004JC002398.

Bromirski, P. D., A. J. Miller, R. E. Flick, and G. Auad (2011), Dynamical suppression of sea level rise along the Pacific coast of North America: Indications for imminent acceleration, *J. Geophys. Res.*, *116*, C07005, doi:10.1029/2010JC006759.

Bromirski, P. D., D. R. Cayan, N. Graham, R. E. Flick, and M. Tyree (2012), *Coastal Flooding-Potential Projections: 2000–2100*, 54 pp., Scripps Inst. of Oceanogr., Calif. Energy Comm., La Jolla, Calif. [Available at ftp://ftp.iod.ucsd.edu/peter/Bromirski_etal_Coastal_Flooding_Potential_PIER_CVAS_2012.pdf.].

Caires, S., A. Sterl, J.-R. Bidlot, N. Graham, and V. Swail (2004), Intercomparison of different wind-wave reanalyses, *J. Clim.*, *17*(10), 1893–1913.

Cayan, D. R., P. D. Bromirski, K. Hayhoe, M. Tyree, M. D. Dettinger, and R. E. Flick (2008), Climate change projections of sea level extremes along the California coast, *Clim. Change*, *87*, 57–73, doi:10.1007/s10584-007-9376-7.

Chang, E. K. M. (2007), Assessing the increasing trend in Northern Hemisphere winter storm track activity using surface ship observations and a statistical storm track model, *J. Clim.*, *20*, 5607–5628.

Cox, A. T., and V. R. Swail (2001), A global wave hindcast over the period 1958–1997: Validation and climate assessment, *J. Geophys. Res.*, *106*(C2), 2313–2329.

Flick, R. E., J. F. Murray, and L. Ewing (2003), Trends in United States tidal datum statistics and tide range, *J. Waterw. Port Coastal Ocean Eng.*, *129*(4), 155–164.

Gemmrich, J., B. Thomas, and R. Bouchard (2011), Observational changes and trends in northeast Pacific wave records, *Geophys. Res. Lett.*, *38*, L22601, doi:10.1029/2011GL049518.

Gershunov, A., and T. P. Barnett (1998), Interdecadal modulation of ENSO teleconnections, *Bull. Am. Meteorol. Soc.*, *79*(12), 2715–2725.

Graham, N. E. (2005), Coastal Impacts of North Pacific Winter Wave Climate Variability: The Southern California Bight and the Gulf of the Farallones, *Pier Project Rep. CEC-500-2005-018*, Calif. Energy Commission Public Interest Energy Research (PIER) Prog., Scripps Inst. of Oceangr. and Hydrol. Res. Cent., San Diego, Calif.

Graham, N. E., and H. F. Diaz (2001), Evidence for intensification of North Pacific winter cyclones since 1948, *Bull. Am. Meteorol. Soc.*, *82*(9), 1869–1893.

Hemer, M. A., J. A. Church, and J. R. Hunter (2010), Variability and trends in the directional wave climate of the Southern Hemisphere, *Int. J. Climatol.*, *30*, 475–491, doi:10:1002/joc.1900.

Hines, W. H., and D. C. Montgomery (1980), *Probability and Statistics in Engineering and Management Science*, 634 pp., John Wiley, New York.

IPCC (2007), Climate Change 2007: Synthesis Report, Assessment Report, edited by Core Writing Team, R. K. Pachauri, and A. Reisinger, Rep. AR4, 104 pp., Intergov. Panel on Clim. Change, Geneva, Switzerland.

Kalnay, E., et al. (1996), The NCEP/NCAR 40-year reanalysis project, *Bull. Am. Meteorol. Soc.*, *77*, 437–471.

Kinsman, B. (1965), *Wind Waves: Their Generation and Propagation on the Ocean Surface*, 676 pp., Prentice Hall, Englewood Cliffs, N. J.

Kumar, A., and M. P. Hoerling (2003), The nature and caused for the delayed atmospheric response to El Nino, *J. Clim.*, *16*, 1391–1403.

Latif, M., and T. P. Barnett (1994), Causes of decadal climate variability over the North Pacific and North America, *Science*, *266*, 635–637.

Latif, M., and T. P. Barnett (1996), Decadal climate predictability over the North Pacific and North America: Dynamics and predictability, *J. Clim.*, *9*, 2407–2423.

Mantua, N. J., and S. R. Hare (2002), The Pacific decadal oscillation, *J. Oceanogr.*, *58*, 35–44.

Mantua, N. J., S. R. Hare, Y. Zhang, J. M. Wallace, and R. C. Francis (1997), A Pacific interdecadal climate oscillation with impact on salmon production, *Bull. Am. Meteorol. Soc.*, *78*, 1069–1079.

McCabe, G. J., M. P. Clark, and M. C. Serreze (2001), Trends in northern hemisphere surface cyclone frequency and intensity, *J. Clim.*, *14*, 2763–2768.

Merrifield, M. A. (2011), A shift in western tropical Pacific sea level trends during the 1990s, *J. Clim.*, *24*(15), 4126–4138.

Miller, A. J., D. R. Cayan, T. P. Barnett, N. E. Graham, and J. M. Oberhuber (1994), The 1976–77 climate regime shift of the Pacific Ocean, *Oceanography*, *7*, 21–26.

O'Reilly, W. C., and R. T. Guza (1991), A comparison of spectral refraction and refraction-diffraction wave propagation models, *J. Waterw. Port Coastal Ocean Eng.*, *117*(3), 199–215.

Pierson, W. J., Jr., and L. Moskowitz (1964), A proposed spectral form for fully developed wind seas based on the similarity theory of S.A. Kitaigorodskii, *J. Geophys. Res.*, *69*(24), 5181–5190.

Ruggiero, P., P. D. Komar, and J. C. Allan (2010), Increasing wave heights and extreme value projections: The wave climate of the U.S. Pacific Northwest, *Coastal Eng.*, *57*, 539–552.

Sasaki, W., S. I. Iwasaki, T. Matsuura, and S. Iizuka (2005), Recent increase in summertime extreme wave heights in the western North Pacific, *Geophys. Res. Lett.*, *32*, L15607, doi:10.1029/2005GL023722.

Seymour, R. J. (2011), Evidence for changes to the northeast Pacific wave climate, *J. Coastal Res.*, *27*(1), 194–201, doi:10.2112/JCOASTRES-D-09–00149.1.

Steele, K. E., J. C. Lau, and Y. L. Hsu (1985), Theory and application of calibration techniques for an NDBC directional wave measurements buoy, *IEEE J. Oceanic Eng.*, *10*, 382–396.

Sterl, A. (2004), On the (in)homogeneity of reanalysis products, *J. Clim.*, *17*, 3866–3873.

Stockdon, H. F., R. A. Holman, P. A. Howd, and A. H. Sallenger (2006), Empirical parameterization of setup, swash, and runup, *Coastal Eng.*, *53*, 573–588.

Storlazzi, C. D., and G. B. Griggs (2000), Influence of El Niño-Southern Oscillation (ENSO) events on the evolution of central California's shoreline, *Geol. Soc. Am. Bull.*, *112*(2), 236–249.

Tolman, H. L. (2009), User Manual and System Documentation of WAVEWATCH III, Version 3.14, Technical Note, U.S. Dep. of Commerce, NOAA, NWS, NCEP, Ocean Model. Branch Contrib., Camp Springs, Md.

Trenberth, K. E., and J. W. Hurrell (1994), Decadal atmosphere-ocean variations in the Pacific, *Clim. Dyn.*, *9*, 303–319.

Wallace, J. M., and D. S. Gutzler (1981), Teleconnections in the geopotential height field during the Northern Hemisphere winter, *Mon. Weather Rev.*, *109*, 784–812.

Wang, X. L., and V. R. Swail (2001), Changes of extreme wave heights in northern hemisphere oceans and related atmospheric circulation regimes, *J. Clim.*, *14*, 2204–2221.

Wang, X. L., V. R. Swail, and F. W. Zwiers (2006), Climatology and changes of extra-tropical cyclone activity: Comparison of ERA-40 with NCEP/NCAR reanalysis for 1958–2001, *J. Clim.*, *19*, 3145–3166, doi:10.1175/JCLI3781.1.

Wang, X. L., V. R. Swail, F. W. Zwiers, X. Zhang, and Y. Feng (2009), Detection of external influence on trends of atmospheric storminess and ocean wave heights, *Clim. Dyn.*, *32*, 189–203, doi:10.1007/s00382-008-0442-2.

Wessel, P., and W. H. F. Smith (1996), A global, self-consistent, hierarchical, high-resolution shoreline database, *J. Geophys. Res.*, *101*(B4), 8741–8743.

Wolter, K., and M. S. Timlin (1998), Measuring the strength of ENSO events—how does 1997/98 rank?, *Weather*, *53*, 315–324.

Young, I. R., S. Zieger, and A. V. Babanin (2011), Global trends in wind speed and wave height, *Science*, *332*(6028), 451–455, doi:10.1126/science.1197219.